OC6 Project Phase IV: Validation of Numerical Models for Novel Floating Offshore Wind Support Structures

Roger Bergua[1], Will Wiley[1], Amy Robertson[1], Jason Jonkman[1], Cédric Brun[2], Jean-Philippe Pineau[2], Quan Qian[3], Wen Maoshi[3], Alec Beardsell[4], Joshua Cutler[4], Fabio Pierella[5], Christian Anker Hansen[5], Wei Shi[6], Jie Fu[6], Lehan Hu[6], Prokopios Vlachogiannis[7], Christophe Peyrard[7], Christopher Simon Wright[8], Dallán Friel[8], Øyvind Waage Hanssen-Bauer[9], Carlos Renan dos Santos[9], Eelco Frickel[10], Hafizul Islam[10], Arjen Koop[10], Zhiqiang Hu[11], Jihuai Yang[11], Tristan Quideau[12], Violette Harnois[12], Kelsey Shaler[13], Stefan Netzband[14], Daniel Alarcón[15], Pau Trubat[15], Aengus Connolly[16], Seán B. Leen[17], Oisín Conway[17]

[1]National Wind Technology Center, National Renewable Energy Laboratory, Golden, CO 80401, USA
[2]Research Department, Bureau Veritas – Marine Division, Saint-Herblain, 44818, France
[3]Research Institute, CSSC Haizhuang Windpower Co. Ltd, Chongqing, 401122, China
[4]Turbine Engineering, DNV, Bristol, BS2 0PS, UK
[5]Department of Wind Energy and Energy Systems, Technical University of Denmark, Lyngby, 2800, Denmark
[6]State Key Laboratory of Coastal and Offshore Engineering, Dalian University of Technology, Dalian, 116024, China
[7]R&D National Hydraulics and Environment Laboratory (LNHE), EDF, Chatou, 78400, France
[8]Gavin & Doherty Geosolutions Ltd., Dublin, D14 X627, Ireland
[9]Institute for Energy Technology, Kjeller, 2007, Norway
[10]Maritime Research Institute Netherlands (MARIN), Wageningen, 6708 PM, The Netherlands
[11]School of Engineering, Newcastle University, Newcastle upon Tyne, NE1 7RU, UK
[12]Floating Offshore Group, PRINCIPIA, La Ciotat 13600, France
[13]Power and Technology Department, Shell International Exploration and Production, Houston, TX 77079, USA
[14]Fluid Dynamics and Ship Theory, Hamburg University of Technology, Hamburg, 21073, Germany
[15]Department of Civil and Environmental Engineering, Universitat Politècnica de Catalunya, Barcelona, 08034, Spain
[16]Department of Offshore Wind, Wood Group Kenny, Galway, H91 R9YR, Ireland
[17]Department of Mechanical Engineering, School of Engineering, University of Galway, Galway, H91 HX31, Ireland

Correspondence to: Roger Bergua (roger.bergua@nrel.gov)

Abstract. This paper provides a summary of the work done within Phase IV of the Offshore Code Comparison Collaboration, Continued, with Correlation and unCertainty (OC6) project, under International Energy Agency Wind Technology Collaboration Programme Task 30. This phase focused on validating the loading on and motion of a novel floating offshore wind system. Numerical models of a 3.6-MW horizontal-axis wind turbine atop the TetraSpar floating support structure were compared using measurement data from a 1:43 Froude-scale test performed in the University of Maine's Alfond Wind-Wave (W2) Ocean Engineering Laboratory. Participants in the project ran a series of simulations, including system equilibrium, surge offsets, free-decays, wind-only conditions, wave-only conditions, and a combination of wind and wave conditions. Validation of the models was performed by comparing the aerodynamic loading, floating support structure motion, tower base loading, mooring line tensions, and keel line tensions. The results show a good estimation of the aerodynamic loading and a reasonable estimation of the platform motion and tower base fore-aft bending moment. However, there is a significant

dispersion in the dynamic loading for the upwind mooring line. Very good agreement was observed between most of the numerical models and the experiment for the keel line tensions.

1 Introduction

The objective of Phase IV of the Offshore Code Comparison Collaboration, Continued, with Correlation and unCertainty (OC6) project is to evaluate the accuracy of load predictions and motions by modeling tools for a novel floating offshore wind turbine (FOWT).

The OC6 project is part of an ongoing effort under the International Energy Agency Wind Technology Collaboration Programme (IEA Wind) Task 30 to verify and validate offshore wind turbine modeling tools (IEA Wind). The foundational OC3 (Offshore Code Comparison Collaboration) project originated back in 2005 as a verification of simulation tools capable of predicting the coupled dynamic loads and responses of FOWTs. Modeling tools that can accurately predict the loading are necessary to enable more reliable and optimized designs. The OC3 project (Jonkman and Musial, 2010) and its extension, OC4 project (Popko et al., 2012; Robertson et al., 2013), focused on code-to-code comparisons for several fixed-bottom (monopile, tripod, jacket) and floating (spar buoy, semisubmersible) designs. The OC5 project (Robertson et al., 2015; Robertson et al., 2016; Robertson et al., 2017; Popko et al., 2018; Popko et al., 2019) compared simulation results to tank test data and measurements from a wind turbine in the Alpha Ventus offshore wind farm. The OC6 project focused on differences observed in previous projects between model predictions and measurements or phenomena not well understood. The first phase (Robertson et al., 2020; Wang et al., 2021) studied the loads associated to the slow-period surge and pitch motions in FOWTs, which are excited through nonlinear wave loading. The second phase (Bergua et al., 2022a) focused on incorporating a more accurate soil/structure interaction model into the simulation tools, able to better represent the boundary conditions and damping in fixed-bottom systems. The third phase (Bergua et al., 2022b) focused on validating the rotor aerodynamic loading for a FOWT undergoing large motions in the surge and pitch directions caused by the floating support structure. The implications of those large motions were also investigated for the near and far wake behavior (Cioni et al, 2023). The fourth phase is focused on validating the coupled dynamics of a novel floating wind design with a streamlined floating support structure, different from traditional FOWT designs. It is also the first time, in these projects, that load predictions for the internal loading within the floating support structure are provided and compared to measurements.

Participants in OC6 Phase IV modeled a 1:43 scaled version of a 3.6-MW wind turbine atop the TetraSpar floating support structure designed by Stiesdal Offshore Technologies. The scaled model tested is representative of the full-scale demonstration project that was installed in Norway in July 2021 (Stiesdal Offshore Technologies). The testing campaign was performed by the University of Maine (Allen & Fowler, 2019). The OC6 Phase IV project followed a stepwise validation approach where the complexity was increased one step at a time to identify and understand potential differences between the experiment and the numerical models (validation) or differences between the numerical models (verification).

The group ran a series of simulations, including system equilibrium, surge offsets, free-decays, wind-only conditions, wave-
70 only conditions, and a combination of wind and wave conditions. This paper summarizes the work done within the OC6 Phase
IV project.

The organization of the remainder of the paper is as follows: Section 2 provides a description of the scaled model and the
testing performed. Section 3 provides a description of the active participants involved in OC6 Phase IV and their modeling
approach. Section 4 then summarizes the load cases that were performed for the verification and validation. Finally, Sections
75 5 and 6 provide some example results from the project and the conclusions drawn.

2 Model Definition

To validate the accuracy of predicting the loading and motion of a novel FOWT, measurement data from an experimental
campaign conducted at the Harold Alfond Wind-Wave (W2) Ocean Engineering Laboratory of the Advanced Structures and
Composites Center at the University of Maine (University of Maine) in December 2018 (Borg, 2019) was used. All the
80 quantities in this section are given at full scale, except when specified otherwise. The basin is 30 m long, 9 m wide, and 5 m
deep (model scale), and is equipped with a 16-paddle wave maker opposite a beach and a bank of fans 7 m wide and 3.5 m tall
(model scale). The testing used a 1:43 Froude-scale thrust-matched model of the 3.6-MW Siemens Gamesa wind turbine, with
a rotor diameter of 129 m, atop the TetraSpar floating support structure (see Figure 1a and Figure 2a). This configuration is
representative of the one used in the full-scale demonstration project (Stiesdal Offshore Technologies).
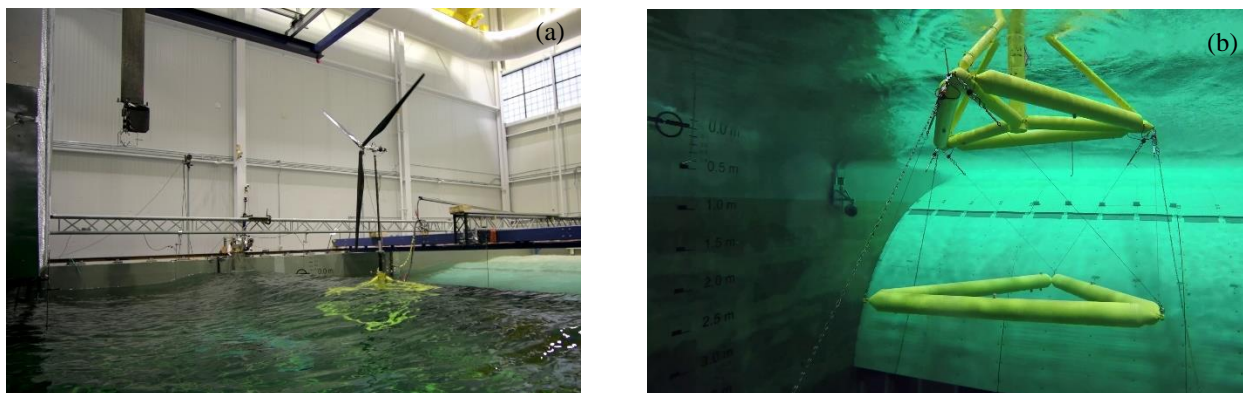
Figure 1: (a) TetraSpar 1:43 scaled model during testing at the University of Maine. (b) Underwater view of the floating support structure. Pictures courtesy of University of Maine.

The TetraSpar is made of two separate structures: hull and keel (see Figure 1b and Figure 2b). The hull consists of a vertical
central column (CC) directly beneath the wind turbine tower. At the base of the central column, there are three radial braces
90 (RB) in the horizontal plane spaced 120° apart. Rigidity is given to this base with hull tri braces (HT) and diagonal braces
(DB). The keel is made of three tri braces (KT) in the horizontal plane. The hull has a tetrahedral shape while the suspended
keel has a triangular shape and acts as a system counterweight. Six taut cables, denoted as keel lines (KL), are used to link the

hull and the keel. The system features a spar-like stability with the whole system center of mass located below the center of buoyancy. The lower the center of mass, the higher the gravitational restoring moments in roll and pitch degrees of freedom.

95   This behavior is achieved thanks to the location of the keel (37.9 m below the hull) and its large mass (80 % of the mass for the complete floating support structure).

All members are cylindrical tubes and most of them are cone-shaped at one end (e.g., RB) or both ends (e.g., DB, HT, and KT). For reference, the HT, KT, and CC cylinders are 4.3 m in diameter. The CC is 32.15 m long, the HT is 52.18 m long, and the KT is 64.30 m long. The hull center of mass is located 13.5 m below the mean sea level while the keel center of mass is

100   located 56.6 m below the mean sea level. The center of buoyancy of the floating support structure is located around 33.8 m below the mean sea level along the CC longitudinal axis. In the physical construction of the system (both at full-scale and model-scale), some members are linked by means of pin joints at one end (e.g., RB in the connection with the central column) or both ends (e.g., DB, and HT). The pin joints allow one rotational degree of freedom. This implies that bending moments in one direction would not be transferred through the kinematic joint. This consideration would be important to study the loading

105   within the hull. However, for this validation campaign, the structural properties (e.g., members thickness distribution) were not known and, therefore, it was not possible to assess such internal loading. Accordingly, participants considered the hull and keel as distinct rigid bodies and only included the flexibility of the keel lines within the floater. The definition document of the OC6 Phase IV project (Wiley et al., 2023) provides information about the length and external diameter for all members (necessary to characterize the hydrostatic and hydrodynamic loads), the equivalent lumped mass and inertia for the hull and

110   the keel to be included as rigid bodies, and the material properties for the keel lines. The total mass of the floating support structure (including the fairlead tension sensors) is 5.66×10^6 kg and the buoyancy is 6.13×10^7 N.
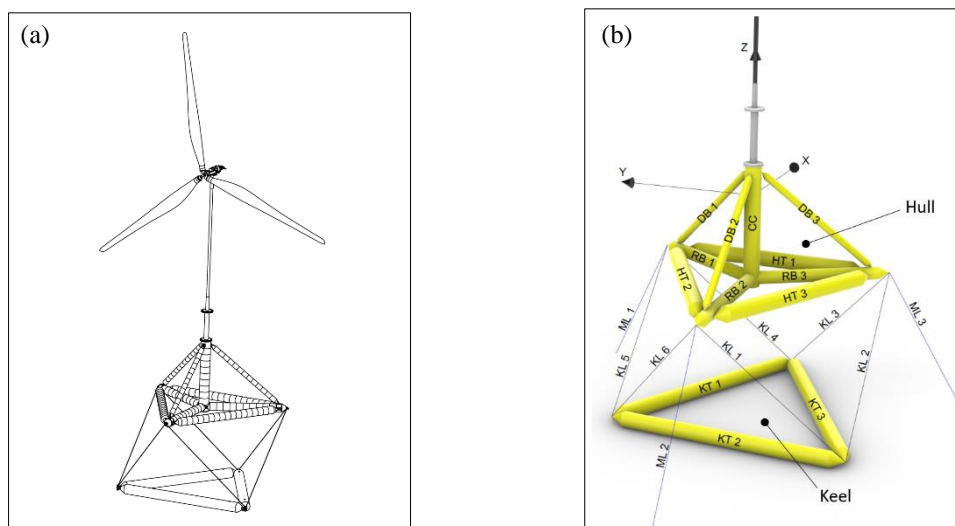
Figure 2: (a) Schematic representation of the model-scale system. (b) View of the TetraSpar floating support structure, with the nomenclature and coordinate system used in the project.

115 The mooring system consisted of three catenary lines (ML1, ML2, and ML3 in Figure 2b). Each of the three lines was made of two different sections: a lower section made of heavier chain and an upper section of lighter chain. The connection between the upper and lower chains for the upwind line (mooring line 2) was near the wave tank floor. This condition may be challenging for some numerical models because it makes the catenary equations more difficult to solve. The two downwind lines (mooring lines 1 and 3) had to be truncated in the testing due to space limitations in the wave tank. The same configuration

120 was replicated in the numerical models. The water depth considered is 193.5 m. The upwind mooring line has a total length around 700 m while the two downwind lines are around 300 m in length, each.

During the testing, one umbilical cable was used to transfer data and power between the system and the carriage in the wave basin. The presence of this umbilical had a large impact on the surge restoring force relative to that of the mooring system. This results in a significant shift of the surge eigenfrequency and change of the system dynamics. Therefore, one additional

125 line was included in the numerical models to account for the umbilical. Detailed dimensions and properties for the mooring lines as well as the umbilical can be found in the definition document (Wiley et al., 2023).

The tower in the model test was made of aluminum and carbon fiber and was built to match a Froude-scaled first tower-bending eigenfrequency of the full-scale design. The sectional properties as well as the material properties are provided in the definition document (Wiley et al., 2023). The tower length is around 76 m, and its mass is 1.51×10^5 kg. Hammer impact tests were

130 performed to check the first tower-bending eigenfrequency. The rotor-nacelle-assembly (RNA) was present in these tests. The first tower-bending frequency for a cantilevered condition (fixed-free) was 0.34-0.35 Hz. For the floating body (free-free) boundary condition, it is expected that this tower bending eigenfrequency will be slightly higher (but this was not tested directly).

The blades used in the testing were made of carbon fiber and were considered as rigid in the numerical models. The blades are

135 61.1 m long and have a mass of 1.9×10^4 kg. Information about the blade properties (e.g., twist, chord length, and airfoil thickness-to-chord ratio along the blade), airfoil polars (i.e., lift and drag coefficients for different angles of attack), blades mass, and blades center of gravity were provided in the definition document (Wiley et al., 2023). Properties of the nacelle as well as the complete RNA are also available in the definition document. The rotor shaft tilt angle is 0° and the RNA mass is 2.62×10^5 kg. The total mass for the system (RNA, tower, and floating support structure including the fairlead tension sensors)

140 is 6.08×10^6 kg and the center of mass is located around 39.9 m below the mean sea level.

The instrumentation during the testing that was used for this validation campaign measured structural loads (e.g., tower base bending moments, keel line tensions, and fairlead tensions in the mooring lines), accelerations (e.g., tower top), tracking motion (e.g., keel and hull six degrees of freedom), and environmental conditions (e.g., wave elevation and wind speed). A complete list of the sensors used during the experimental campaign is also available in the definition document (Wiley et al., 2023).

3 Participants and Modeling Approach

A total of 17 academic and industrial partners from 10 different countries participated in the OC6 Phase IV project. Those actively involved were Bureau Veritas (BVMO, France), China State Shipbuilding Corporation (CSSC, China), Det Norsk Veritas (DNV, United Kingdom), Technical University of Denmark (DTU, Denmark), Dalian University of Technology (DUT, China), Électricité de France (EDF, France), Gavin & Doherty Geosolutions Ltd (GDG, Ireland), Institute for Energy Technology (IFE, Norway), Maritime Research Institute Netherlands (MAR, The Netherlands), National Renewable Energy Laboratory (NREL, United States of America), Newcastle University (NU, United Kingdom), PRINCIPIA (PRI, France), Shell (SHELL, United States of America), Hamburg University of Technology (TUHH, Germany), Universitat Politècnica de Catalunya (UPC, Spain), and Wood and University of Galway (W&UG, Ireland).

The system studied in OC6 Phase IV requires a coupled aero-hydro-elastic approach. The participants used modeling approaches of different fidelity for the structural dynamics, aerodynamics, and hydrodynamics. Some participants decided to use more than one modeling approach, and some used different codes. A total of 19 numerical models were involved in this verification and validation campaign. A list of the participants, codes, and the structural approach adopted is provided in Table 1. Most participants included the tower and keel lines flexibility in their numerical models and can obtain the internal loading. Participants modelledd the tower using a finite-element model (e.g., by means of a beam theory). Several participants then performed a modal reduction (e.g., Craig-Bampton method (Craig and Bampton, 1968)) to improve the computational efficiency. Different approaches can be adopted to model the keel lines depending on the code capabilities. For example, from higher to lower fidelity: cable elements, nonlinear springs, linear springs, or slender beams. Cable elements yield forces in tension and account for the proper mass distribution and line sagging. The nonlinear springs approach can potentially reproduce the same stiffness behavior, but the cable mass distribution is not included. Unlike the nonlinear springs approach, the linear springs yield forces in tension and compression (which is unphysical). The slender beam approach can provide the desired linear axial stiffness under tension and distributed mass. However, it yields forces at compression and introduces some small stiffness in undesired directions (e.g., shear, bending, and torsion) not seen in the keel lines. Slack events in the keel lines require the use of a nonlinear approach (e.g., cable elements or nonlinear springs). However, potential slack in the keel lines have not been observed during the testing (Borg, 2019) and any of the above proposed approaches should provide similar results.

NREL used two numerical models with the only difference being the structural approach adopted. Similar to OC6 Phase II (Bergua et al., 2022a), NREL1 models the tower in the ElastoDyn module and the substructure (i.e., floater) in the SubDyn module while NREL2 models the tower and substructure in the SubDyn module. The SubDyn module of OpenFAST makes use of a modal reduction. When performing a modal reduction by means of the Craig–Bampton approach for a fixed-bottom system (e.g., system studied in the OC6 Phase II project) in SubDyn, the Guyan modes (also known as boundary modes) provide information about the static deflection of the body and the Craig-Bampton modes (also known as internal or normal modes) provide information about the inherent dynamics. The Guyan modes are obtained with the interface node free while

the Craig-Bampton modes are obtained with the interface node fixed. When computing the Guyan and Craig-Bampton modes, the bottom (reaction node) is fixed or it accounts for the foundation compliance. For a floating system, the formulation is different. In this case, the Guyan modes capture the rigid body motion because there is no reaction node, and the Craig-Bampton modes (interface node fixed) capture the elastic modes. For a floating system, the elastic modes and the applied loads (e.g., gravity acceleration, hydrostatic loading, hydrodynamic loading) in OpenFAST are expressed in a floating frame of reference. It is important to note that the applied loads are computed based on the Guyan modes (rigid body motion for a floating system). Only the mooring loads in OpenFAST are computed based on the combined Guyan and Craig-Bampton

185 modes (i.e., rigid body motion and elastic deflections in the substructure). For the above reasons, when modeling floating systems in OpenFAST, it is recommended to avoid including in SubDyn bodies that experience significant elastic deflections. Accordingly, the NREL2 model can be considered of lower fidelity than NREL1. Other participants using the OpenFAST code (e.g., DUT1 and SHELL) adopted a similar approach to NREL1. W&UG included the structural part in Flexcom rather than OpenFAST. Flexcom does not perform a modal reduction, and instead computes the solution in the time domain using a direct

190 integration method.

Most participants used a dynamic approach to account for the mooring lines in their numerical models (Table 1). The mooring line dynamic approach is usually based on a lumped mass approach where the lines are discretized into concentrated masses connected by massless springs with dampers in parallel. Only four participants (BVMO, DNV, NU, and UPC) used a quasi-static approach. For BVMO, NU, and UPC the quasi-static approach relies on catenary formulations to compute the mooring

195 line shape and tension at every time step assuming instantaneous static equilibrium. DNV uses a pre-computed lookup table with the quasi-static fairlead forces based on horizontal and vertical displacements. The main disadvantage of the quasi-static approach is that it neglects the mooring line inertial forces and the hydrodynamics (e.g., drag and added mass). The quasi-static approach may have difficulties reproducing the proper behavior when the line experiences significant motions or dynamic events (e.g., snap loads when a line becomes slack and it is suddenly under tension again, as observed in OC5 Phase

200 II project (Robertson et al., 2017)).

Table 1: Summary of participants, codes, and structural approach

Participant	Code	Structural flexibility		Mooring lines	
		Tower	Keel Lines	Quasi-static	Dynamic
BVMO	Opera		✓	✓	
CSSC	HAWC2	✓	✓		✓
DNV	Bladed	✓	✓	✓	
DTU	HAWC2	✓	✓		✓
DUT1	OpenFAST	✓	✓		✓
DUT2	SIMA	✓	✓		✓
EDF	DIEGO	✓	✓		✓

GDG	OrcaFlex	✓	✓		✓
IFE	3dFloat	✓	✓		✓
MAR1	aNySIM-XMF	✓	✓		✓
MAR2	ReFRESCO & aNySIM-XMF				✓
NREL1	OpenFAST	✓	✓		✓
NREL2	OpenFAST	✓	✓		✓
NU	DARwind	✓		✓	
PRI	Deeplines Wind	✓	✓		✓
SHELL	OpenFAST	✓	✓		✓
TUHH	panMARE				✓
UPC	FloawDyn	✓	✓	✓	
W&UG	Flexcom & OpenFAST	✓	✓		✓

Table 2 provides a list of the participants, codes, and the aerodynamic approach used. Participants in the project used models of different fidelity: blade element momentum (BEM) theory, free vortex wake (FVW) methods, and computational fluid

205   dynamics (CFD). All BEM and FVW models used by participants are based on the lifting line theory. The airfoil polar data provided in the definition document was used as input for these numerical models. The BEM approach relies on several corrections (e.g., dynamic inflow, skewed wake, blade-root and blade-tip losses, unsteady airfoil aerodynamics) to address the rotor aerodynamics and subsequent loads in different wind turbine operating conditions. Higher fidelity models like FVW and CFD inherently account for these effects and are better suited to study situations like skewed flow caused by yawed inflow or

210   rotor tilt. Moreover, these higher fidelity models can provide insights about the wake behavior. MAR2 used a blade-resolved CFD approach and it used a surface mesh based on the blade geometry provided by the University of Maine.

The numerical model used by SHELL is the same numerical model as NREL1. The only difference is in terms of the aerodynamic model. SHELL uses a FVW approach while NREL uses a BEM approach. For wind turbines in operating conditions, it is expected that SHELL and NREL1 provide different responses due to the different aerodynamic approach.

215   When the wind turbine is in idling or parked conditions, the aerodynamic induction model is disabled, and SHELL and NREL1 models provide the same response.

Table 2: Summary of participants, codes, and aerodynamic approach

Participant	Code	Aerodynamic approach		
		BEM	FVW	CFD
BVMO	Opera	✓		
CSSC	HAWC2	✓		

DNV	Bladed	✓	
DTU	HAWC2	✓	
DUT1	OpenFAST	✓	
DUT2	SIMA	✓	
EDF	DIEGO	✓	
GDG	OrcaFlex	✓	
IFE	3dFloat	✓	
MAR1	aNySIM-XMF	✓	
MAR2	ReFRESCO & aNySIM-XMF		✓
NREL1	OpenFAST	✓	
NREL2	OpenFAST	✓	
NU	DARwind	✓	
PRI	Deeplines Wind	✓	
SHELL	OpenFAST		✓
TUHH	panMARE		✓
UPC	FloawDyn	✓	
W&UG	Flexcom & OpenFAST	✓	

The TetraSpar floating support structure design is made of slender members. Due to the nature of the system, it is possible to use strip theory (e.g., using Morison's equation (ME)) to model the hydrodynamic loading. For a floating system, it is necessary to account for the relative form of Morison's equation. Assuming, for the sake of simplicity, that the fluid and structure velocity are colinear and normal to the member, the relative form of Morison equation can be expressed as Eq. 1.

$$F = \frac{1}{2} \cdot C_d \cdot \rho \cdot D \cdot (u_w - u_s) \cdot |u_w - u_s| + C_p \cdot \rho \cdot \frac{\pi \cdot D^2}{4} \cdot \dot{u}_w + C_a \cdot \rho \cdot \frac{\pi \cdot D^2}{4} \cdot \dot{u}_w - C_a \cdot \rho \cdot \frac{\pi \cdot D^2}{4} \cdot \dot{u}_s \qquad (1)$$

where F is the force per unit length, u_w is the fluid velocity, u_s is the structure velocity, $\dot{u}_w$ is the fluid acceleration, $\dot{u}_s$ is the structure acceleration, D is the cylinder outer diameter, ρ is the fluid density, C_d is the drag coefficient, C_p is the wave dynamic pressure coefficient (1 for circular members), and C_a is the added mass coefficient. The inertia coefficient (C_m) is related to the added mass and the wave dynamic pressure coefficients as follows: $C_m = C_a + C_p$.

The first term in Eq. 1 corresponds to the drag force (that includes wave excitation forcing and damping), the second term corresponds to the Froude-Krylov force, the third term is the scattering force, and the fourth term is the added mass component. The combination of Froude-Krylov and scattering forces can also be referred as the fluid inertia force.

Alternatively, it is possible to study the system by means of the boundary element method based on the potential flow (PF) theory. In general, this method is used for large volume structures and assumes small motions around the equilibrium position. The hydrodynamic properties are obtained in frequency-domain in tools like WAMIT (Lee and Newman, 2006), NEMOH (Babarit and Delhommeau, 2015), or HAMS (Liu, 2019) that compute the wave diffraction and radiation for three-dimensional

235   floating structures.

Table 3 shows a comparison between the strip theory and the PF theory. The PF theory does not include viscous drag effects. To overcome this limitation, it is possible to use a hybrid model that accounts for the radiation-diffraction solution from the PF theory and Morison-based elements for the drag forces.

Table 3: Comparison between strip and potential flow theories

Physics		Strip theory	Potential flow theory
Drag forces		Constant drag coefficient	None
Inertial forces	Froude-Krylov	Constant dynamic pressure coefficient	Frequency dependent
	Scattering forces	Constant added mass coefficient	
	Added mass	Constant added mass coefficient	Frequency dependent
Damping forces	Linear	None	Frequency dependent radiation
	Quadratic	Viscous damping from drag forces	None
Hydrostatic restoring		Linear or nonlinear	Linear

240

Table 4 provides a list of the participants, codes, and the hydrodynamic approach used. Most participants modeled the TetraSpar system by means of the ME. Participants using the PF theory, except NU, included the viscous drag component from Morison-based members. Some participants (BVMO) used the linear PF data for radiation and diffraction, and added the second-order sum and difference frequency forces. These second-order terms (2nd PF) are nonlinear effects able to excite the

245   floating system out of the wave linear region (covered by the 1st PF). The difference-frequency forces account for the low frequency range, including the mean and slow drift. The sum-frequency forces can excite the floating system above the linear wave region. It is also important to note that the TetraSpar design has two bodies: hull and keel. To get the loads at the keel lines, it is necessary to discretize the system into at least two bodies. Some participants using the PF method included two potential flow bodies in their numerical models while others included the hull as a potential flow body and the keel as Morison

250   elements.

Regarding the wave theory used, some participants used a linear superposition of Airy waves while others also included second-order wave kinematics (Sharma and Dean, 1981). Wave stretching allows for the wave kinematics and hydrodynamic loads to be computed at all nodes up to the instantaneous free surface, unlike models without wave stretching, which compute wave kinematics and loads at nodes up to the mean sea level regardless of a wave crest or trough at a given time. Second-order

255 wave kinematics and wave stretching are an extension to the strip-theory solution, and it is only considered by ME and hybrid models (ME+PF).

Some participants (IFE, MAR1, NREL, PRI, SHELL, TUHH, and UPC) prescribed the wave elevation time series in their simulations while other participants used statistical information to generate the waves (potentially with random phasing that does not match the experiment).

260

Table 4: Summary of participants, codes, and hydrodynamic approach

Partici pant	Code	Hydrodynamics				Wave theory		Wave stretching
		ME	1st PF	2nd PF	CFD	1st order	1st & 2nd order	
BVMO	Opera	✓	✓	✓		✓		
CSSC	HAWC2	✓					✓	✓
DNV	Bladed	✓				✓		✓
DTU	HAWC2	✓				✓		✓
DUT1	OpenFAST	✓					✓	
DUT2	SIMA	✓				✓		
EDF	DIEGO	✓				✓		✓
GDG	OrcaFlex	✓				✓		✓
IFE	3dFloat	✓					✓	✓
MAR1	aNySIM-XMF	✓[†]					✓	✓
MAR2	ReFRESCO & aNySIM-XMF				✓		✓	
NREL1	OpenFAST	✓					✓	✓
NREL2	OpenFAST	✓					✓	✓
NU	DARwind		✓					
PRI	Deeplines Wind	✓					✓	✓
SHELL	OpenFAST	✓					✓	✓
TUHH	panMARE	✓	✓				✓	✓
UPC	FloawDyn	✓				✓		✓
W&UG	Flexcom & OpenFAST	✓				✓		✓

[†]Morison-based elements for the hull only account for the drag and Froude-Krylov forces. The added mass, scattering forces, and linear damping are obtained from a hydrodynamic database based on a potential flow solution. It can be considered a hybrid model.

The information provided in Tables 1, 2, and 4 indicates the modeling approach adopted by each participant. Many of the codes used have other capabilities not applied in this project.

265 Numerical models were built at full scale and the results, as well as the measurements and discussion, are presented at full-scale, using Froude scaling to upscale the measurements. MAR2, the only participant using a CFD code, simulated the system at model-scale and upscaled the results using Froude scaling before providing them for comparison. This may allow the CFD approach capture physics that are scale-dependent.

4 Load Cases

270 A stepwise validation procedure was performed in the OC6 Phase IV project taking advantage of the experimental campaign carried out by the University of Maine. The testing campaign used an open-loop control approach, where the rotor speed and the blade pitch angle were held constant.

Table 5 provides a summary of the simulations that are presented in Section 5, including the system equilibrium (Load Case 1.1), wind-only condition for rated thrust considering the floating system (Load Case 3.1) and a fixed boundary condition at

275 the tower base (Load Case 3.4), wave-only conditions considering regular waves (Load Case 4.1), wave-only conditions considering irregular waves (Load Cases 4.2, 4.3, and 4.4), and a combination of wind and wave conditions (Load Cases 5.2, 5.3, and 5.4).

Load case numbering is consistent with past phases of the OC3-OC6 projects. Some numbers are skipped because Table 5 only includes the load cases presented in Section 5. The list of all load cases studied can be found in the definition document

280 (Wiley et al., 2023).

Table 5: Offshore Code Comparison Collaboration, Continued, with Correlation and unCertainty (OC6) Phase IV load case simulations (summary)

	Load Case	Description	Wind Conditions	Marine Conditions	Comparison Type
Static Analysis	1.1	Equilibrium	None	Still water	Static response
Wind Only	3.1	Rated wind (floating platform)	Steady wind V_{hub} = 9.89 m s^{-1} Ω = 12.2 rpm, β = -6.2°	Still water	Steady response
	3.4	Rated wind (fixed platform)	Steady wind V_{hub} = 9.89 m s^{-1} Ω = 12.2 rpm, β = -6.2°	Still water	Steady response
Waves Only	4.1	Post-rated condition	None Ω = 0 rpm, β = 0°	Regular waves: H = 8.31 m, T = 12.41 s	Time series (t = 3,934 s)
	4.2	Rated condition	None Ω = 0 rpm, β = 0°	Irregular waves: JONSWAP wave spectrum H_s = 1.46 m, T_p = 6.73 s, γ = 2.3	Time series (t = 10,977 s)
	4.3	Post-rated condition	None Ω = 0 rpm, β = 0°	Irregular waves: JONSWAP wave spectrum H_s = 8.00 m, T_p = 12.20 s, γ = 2.2	Time series (t = 10,977 s)
	4.4	50-yr storm	None	Irregular waves: JONSWAP wave spectrum	Time series (t = 10,977 s)

	Load Case	Description	Wind Conditions	Marine Conditions	Comparison Type
			Ω = 0 rpm, β = 0°	H_s = 12.81 m, T_p = 15.79 s, γ = 3.3	
Wind and Waves	5.2	Rated condition	Unsteady wind V_{hub} = 9.89 m s⁻¹, TI = 2.4 % Ω = 12.2 rpm, β = -6.2°	Irregular waves: JONSWAP wave spectrum H_s = 1.46 m, T_p = 6.73 s, γ = 2.3	Time series (t = 10,977 s)
	5.3	Post-rated condition	Unsteady wind V_{hub} = 24.05 m s⁻¹, TI = 2.5 % Ω = 13.3 rpm, β = 18.7°	Irregular waves: JONSWAP wave spectrum H_s = 8.00 m, T_p = 12.20 s, γ = 2.2	Time series (t = 10,977 s)
	5.4	50-yr storm	Unsteady wind V_{hub} = 44.62 m s⁻¹, TI = 8.9 % Ω = idling, β = 89°	Irregular waves: JONSWAP wave spectrum H_s = 12.81 m, T_p = 15.79 s, γ = 3.3	Time series (t = 10,977 s)

H: regular wave height	γ: peak-enhancement factor	
H_s: significant wave height	V_{hub}: average hub-height wind speed	β: blade pitch angle
T: regular wave period	TI: turbulence intensity	t: time
T_p: peak-spectral wave period	Ω: rotor speed	

The system equilibrium was studied based on the initial measurements during the testing when the wind or wave loading was not applied yet. During the testing, significant differences in the surge resting position were observed before applying wind and wave loads, depending on the load case (between -6.7 m and +6.4 m from the origin of the coordinate system used). This introduces a significant uncertainty in the experimental results that may also impact the tension observed in the mooring lines, especially in mooring line 2. It is known that the umbilical used during the testing significantly moved the system downwind (around 30 m at full scale). This behavior is also replicated in the numerical models when including the umbilical in the system. However, this large surge offset is less than ideal. The umbilical, as well as the friction of the mooring lines with the bottom of the wave tank, could be introducing some hysteresis that may result in the different system resting conditions observed during the testing. For Load Case 1.1, participants considered still water conditions in their numerical models and reported the static equilibrium of the system.

Load Cases 3.X were used to characterize the wind turbine aerodynamic thrust force. In Load Cases 3.1 and 3.4, the mean wind speed at the hub height was 9.89 m s⁻¹ and the turbulence intensity was 2.4 %. The wind generated in the basin did not include any wind shear. But the wind field did not cover the region next to the water (e.g., floater) due to the location of the fans in the testing. For Load Cases 3.X, participants considered spatially uniform steady winds and did not account for the aerodynamic drag in the floating support structure. During the testing, the rotor speed was kept constant at 12.2 rpm and the blade pitch angle was set to -6.2° to match the target aerodynamic rotor thrust using the tower base bending moment as a proxy sensor.

Load Cases 4.X were used to characterize the hydrodynamics of the system. These load cases were wave-only conditions with the system being loaded by waves, no inflow wind, and with a parked wind turbine condition. Load Case 4.1 considered a regular wave for a severe sea state that can be considered representative of the wind turbine operating in the post-rated region.

The regular wave height considered was 8.31 m and the regular wave period was 12.41 s. Load Cases 4.2, 4.3, and 4.4
305 considered irregular waves. Load Case 4.2 can be considered a moderate sea state representative of the wind turbine operating
at the rated region while Load Case 4.3 can be considered a severe sea state representative of post-rated conditions. Load Case
4.4 addressed the system response for an extreme storm condition with a 50-year return period. The significant wave height
and peak-spectral wave period for these three irregular wave conditions are available in Table 5. In the definition of the testing
campaign, the Torsethaugen wave spectrum was used. The Torsethaugen wave spectrum often features two peak periods
(Torsethaugen and Haver, 2004), but in this case a single peak was observed in the measurements. Accordingly, peak-
enhancement factors chosen to reproduce the proper wave elevation distribution by means of a JONSWAP wave spectrum
were provided to the participants (see Table 5).

Load Cases 5.X dealt with the system response for the combined wind and waves that were studied separately in Load Cases
3.X and Load Cases 4.X. For these load cases, participants considered spatially uniform unsteady winds based on the measured
315 hub-height wind speed in the X-direction.

Testing the 50-year storm condition with wind (i.e., Load Cases 3.3 and 5.4) presented some challenges due to a large yaw
motion of the system. This behavior was not representative of the physical full-scale response. Froude scaling results in low
Reynolds numbers and poor aerodynamic performance, often requiring larger chord lengths than the geometrically scaled
values would suggest. It may be that the large chord lengths used along the scaled blades resulted in higher-than-expected
320 resultant rotor yaw loads in idling conditions. To limit the yaw motion, the University of Maine added a yaw stiffness bridle
for these load cases. Additional insights about this arrangement can be found in the definition document (Wiley et al., 2023).
When simulating the system with the rotor in idling conditions and the yaw bridle in place, several participants (e.g., DNV,
DTU, NREL, W&UG) reported instability issues in their numerical models. The wind turbine experienced a coupled motion
that involved the sway, roll, and yaw degrees of freedom. During idling conditions (89° blade pitch angle), it is recommended
325 to disable the aerodynamic induction model. Moreover, it is also recommended to disable the unsteady airfoil aerodynamics
because the angles of attack along the blade are significant, placing the aerodynamic model in deep dynamic stall conditions
where the conventional unsteady aerodynamic theory is not valid. The instabilities observed in some numerical models
decreased when following these recommended practices, but they did not completely disappear. Some participants (e.g.,
NREL, DNV) decided to impose a constant rotor speed of 0.7 rpm to get rid of this instability. W&UG applied a higher axial
330 stiffness to the yaw bridle (two orders of magnitude stiffer) to alleviate these effects.

5 Results

In this section, a comprehensive overview of the studied load cases shown in Table 5 is presented. Results are presented for
the aerodynamic loading, floating support structure motion, tower base loading, upwind fairlead tension, and keel line tensions.

5.1 Aerodynamic loading

335   Load Cases 3.X focus on ensuring that the aerodynamic models were implemented correctly. During the experimental testing in Load Case 3.1, the blade pitch angle was adjusted to match the rated aerodynamic rotor thrust. The blade pitch angle used during the testing (-6.2°) was also used by the participants as it returned a similar output. Participants considered steady spatially uniform wind in their numerical models while the experiment contains a residual amount of turbulence.

Figure 3 shows the aerodynamic rotor thrust, the fairlead 2 tension, the tower base fore-aft bending moment, and the hull pitch
340   motion. For the experiment, a gray rectangle indicative of two times the standard deviation (2σ) is also included. The aerodynamic rotor thrust was not measured or derived during the testing. The results from the numerical models are compared with each other as a verification. The fairlead 2 tension corresponds to the load measured in the upwind mooring line. As observed, the numerical models predict a lower tension than the experiment. However, the numerical models had excellent agreement when looking at the nonlinear relationship between force and imposed static surge offsets. The higher-than-expected
345   tension for the experiment is likely due to the large surge position of the system in resting conditions before the wind was applied (+6.4 m from the system origin). Regarding the tower base fore-aft bending moment, it was decided to analyse relative magnitudes between the resting condition and the loaded system because the mean bending moment during the testing campaign was not reliable. The same postprocessing was applied for the participant results (i.e., the mean value reported for the equilibrium condition in Load Case 1.1 was subtracted from the reported results). The numerical models tend to slightly
350   overpredict the tower base fore-aft bending moment. This would indicate that the aerodynamic rotor thrust observed by the numerical models is slightly higher than in the experiment. Similarly, the relative hull pitch rotation is compared. The hull motion is tracked at its center of mass. The experiment and most numerical models experience a hull pitch rotation of -2° for the equilibrium condition (Load Case 1.1). When the rated wind condition is applied, the relative pitch rotation is close to 7° or 8°. This means that the hull pitch moves from -2° to 5° or 6°. Similar to the tower base fore-aft bending moments, most numerical models predict a slightly larger rotation than the experiment.
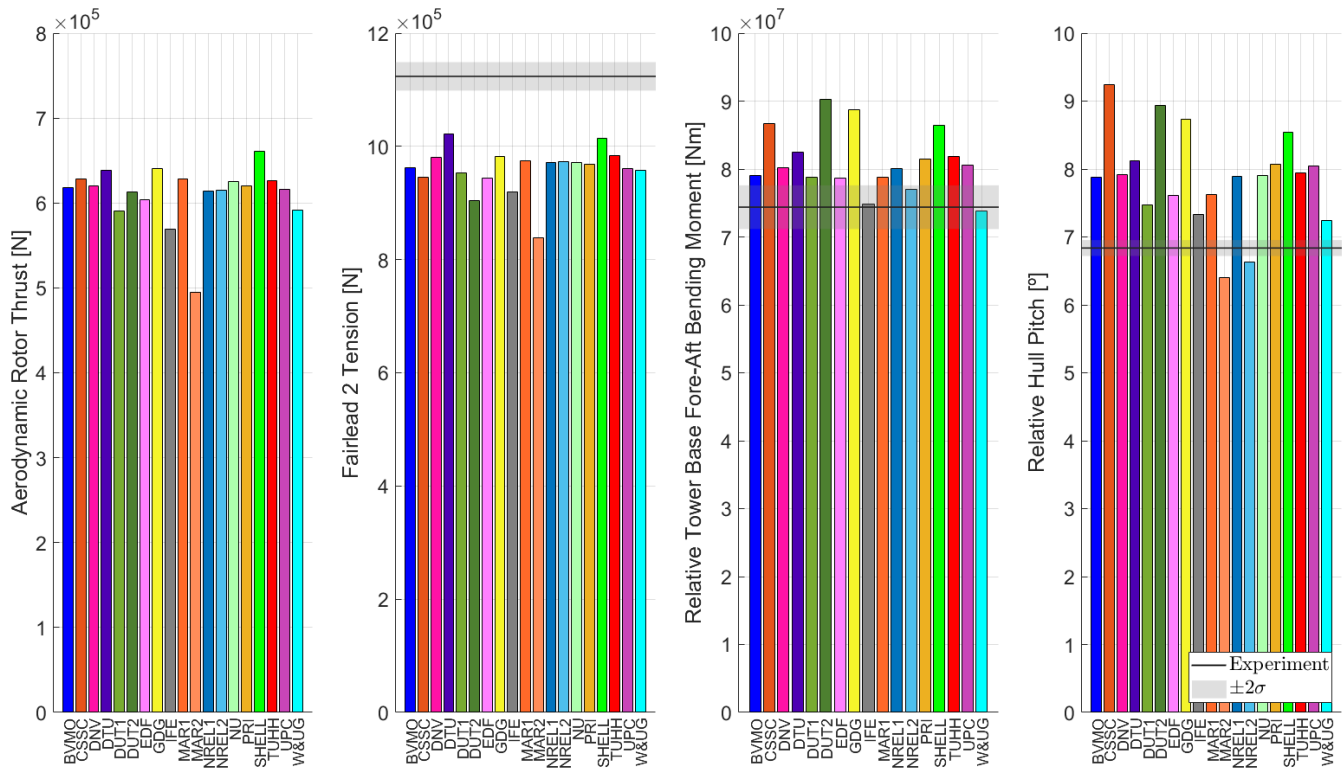
Figure 3: Aerodynamic rotor thrust, fairlead 2 tension, tower base fore-aft bending moment, and hull pitch rotation for rated wind conditions (Load Case 3.1).

360   The unusual blade pitch angle (-6.2°) used during the experiment and replicated by the participants, provides an aerodynamic rotor thrust similar to the target one for most numerical models based on the tower base bending moment shown in Figure 3. However, when looking at the aerodynamic rotor torque (not shown), it was observed that the value is negative for the experiment and the numerical models. This means that the wind turbine had to be powered (i.e., system acting as a motor instead of a generator) to maintain the rotational speed of 12.2 rpm.

365   Figure 4 compares the aerodynamic rotor thrust when considering the floating system (Load Case 3.1) and a fixed boundary condition at the tower base (Load Case 3.4). For reference, Figure 4 also includes the median from participants results for the two boundary conditions. The scaled system and the numerical models do not have a wind turbine tilt angle. In Load Case 3.1, the rotor is tilted according to the hull pitch angle (see Figure 3) and the tower compliance while in Load Case 3.4 the rotor is solely tilted according to the tower compliance. Most numerical models predict a very similar aerodynamic rotor thrust for

370   these two boundary conditions.

    Some higher fidelity models (i.e., FVW and CFD) show some sensitivity to the hull rotation. For example, MAR2 (CFD) experiences a significant reduction (-11.8 %) in the aerodynamic rotor thrust for the floating system. This may be related to some physical effects due to high angles of attack occurring in the simulation. In those conditions, flow separation and stall

may occur leading to lower thrust values. However, it should be noted that the Reynolds numbers at model-scale are low. Flow
375 separation at large angles of attack and the transition from laminar to turbulent flow may not be captured accurately in the
blade-resolved approach at model-scale using the standard k-omega SST turbulence model. An opposite trend is observed for
SHELL (FVW). In this case, the rotor tilt due to the hull pitch rotation results in a slightly higher (+3.6 %) rotor aerodynamic
thrust compared to the fixed platform condition.

Comparing NREL1 and SHELL (same numerical model with different aerodynamic theory) for the fixed platform condition,
380 it can be observed that SHELL (FVW) results in a slightly higher (+3.5 %) rotor aerodynamic thrust than NREL1 (BEM). This
is aligned with the behavior observed in OC6 Phase III project (Bergua et al., 2022b). This difference is likely due to the
slightly different induction factors in the rotor.
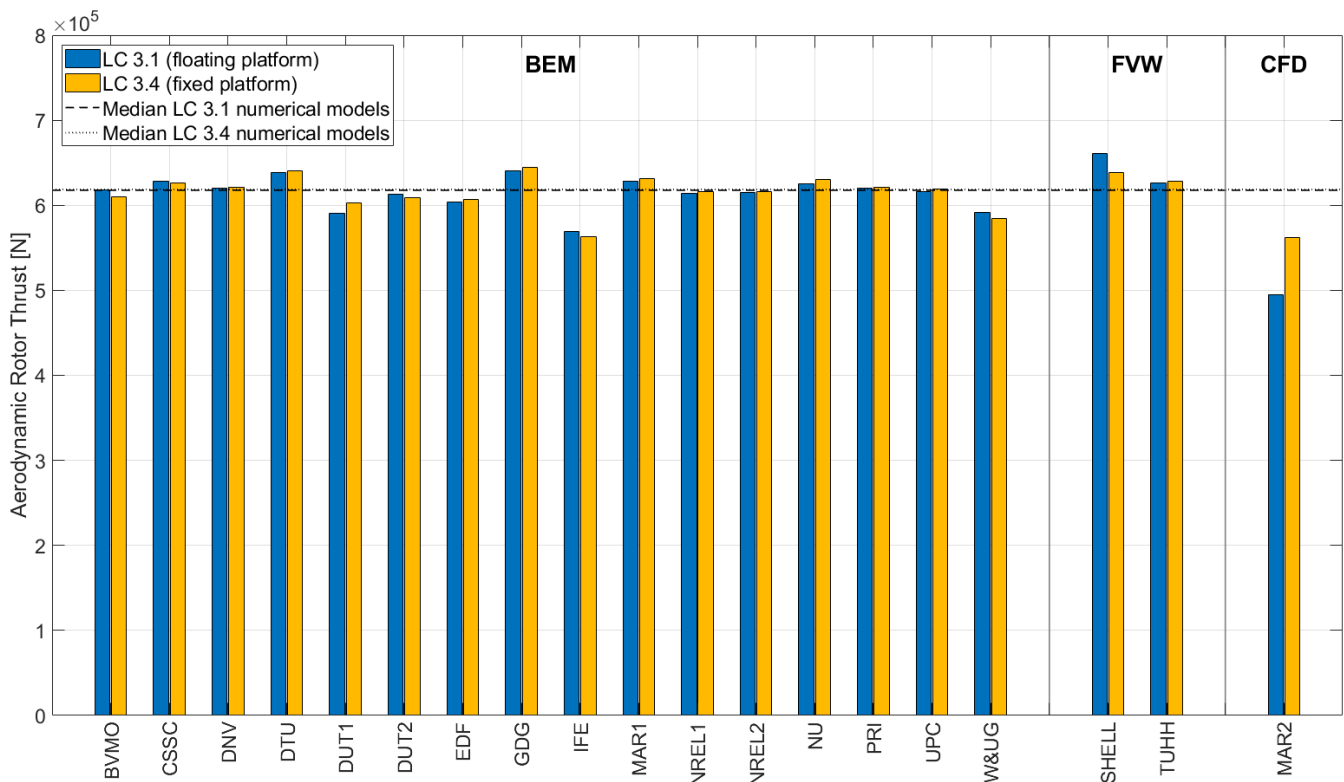
Figure 4: Comparison of aerodynamic rotor thrust for floating (Load Case 3.1) and fixed (Load Case 3.4) conditions. Outputs
385 sorted out according to the aerodynamic theory: blade element momentum (BEM), free vortex wake (FVW), and computational
fluid dynamics (CFD).

5.2 Floating Support Structure Motion

One regular wave-only test was used to examine the wave-structure response of the system. A response amplitude operator
(RAO) for a regular wave is the ratio between the system motion response amplitude to the wave excitation amplitude at the
wave natural frequency. The regular wave studied in the basin is nonlinear (i.e., it contains wave harmonics, and it does not

describe a perfect sinusoid), as such, the RAO is computed based on the fast Fourier transform (FFT) amplitude obtained at the wave natural frequency. Figure 5 shows the RAO for the surge, heave, and pitch degrees of freedom at the hull center of mass using a regular wave for a severe sea state (Load Case 4.1). The figure also includes the experimental results from three repeats performed during the testing. Most numerical models tend to slightly overpredict the surge and heave motions, while

395   the pitch motion is slightly underpredicted. The CFD approach from MAR2 seems to be able to accurately predict the response in the three directions.

Participants initially tuned the hydrodynamic coefficients (i.e., drag and inertia coefficients for ME models and drag coefficients for the hybrid models) based on free decays in still water. However, it is expected that the viscous drag hydrodynamic damping is dependent on the sea state (Pegalajar-Jurado, 2019). Nevertheless, participants in this project used

400   the same hydrodynamic coefficients for all the cases studied.

Based on a sensitivity analysis performed over the ME approach, it was determined that the hull motion response experienced in Load Case 4.1 was mainly driven by the hydrodynamic inertia component. Higher hydrodynamic drag coefficients resulted in slightly higher damping for the system, but the model was not very sensitive. The most slender members (e.g., diagonal braces) have contributions from both drag and inertia while the largest members (e.g., central column) are dominated by inertia.

405   These observations are also aligned with previous studies on the TetraSpar design (Thomsen, 2021). Members near the mean sea level (i.e., central column and diagonal braces) drive the system response as the wave kinematics are strongest in that region and decay exponentially with increasing depth. For reference, most numerical models based on the ME approach used an inertia coefficient equal to 2. This value is also in good agreement with previous studies on the TetraSpar design (Thomsen, 2021).
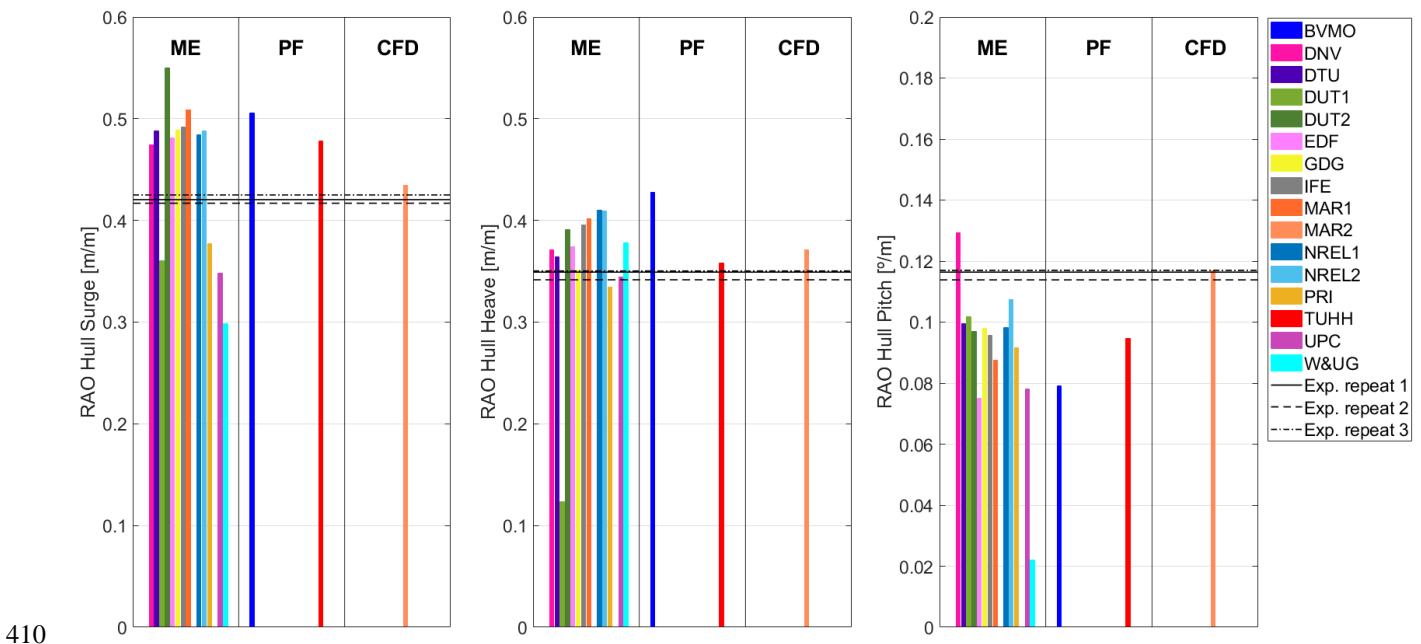
410

Figure 5: Response amplitude operators (RAO) for the surge, heave, and pitch degrees of freedom for a regular wave with a height of 8.31 m and period of 12.41 s (Load Case 4.1). Outputs sorted out according to the hydrodynamic theory: Morison equation (ME), potential flow (PF) augmented with viscous drag, and computational fluid dynamics (CFD).

Figure 6 shows the power spectral density (PSD) of the hull surge motion for the combined unsteady wind and wave condition

415 in Load Case 5.3. The wave height and wave period considered in Load Case 5.3 is comparable in magnitude to the regular wave analysed in Load Case 4.1. In the very low frequency range, rigid body motion activity can be observed around the platform surge eigenfrequency. The response at this frequency is driven by the wind excitation and nonlinear hydrodynamic forces able to excite the system outside the linear wave excitation region (e.g., second-order terms in the PF solution or second-order wave kinematics and wave stretching for the numerical models using Morison-based elements). In this case, the impact

420 of the wave stretching is significantly larger than the impact of including second-order wave kinematics. For the linear wave region (around 0.08 Hz in Figure 6), the results are aligned with the response observed for the regular wave condition. For example, participants slightly overpredicting the response in the regular wave condition (Figure 5) are also showing similar trends for the irregular wave condition (Figure 6). Figure 6 also shows a group of participants (DUT1, DUT2, NU, and W&UG) with a very small response around the platform surge frequency. These participants defined a steady wind condition and,

425 therefore, do not include the wind excitation due to the wind turbulence in the very low frequency region. For NU, using a steady wind condition together with a 1st PF approach for the hydrodynamics, results in a lack of system response in the platform surge eigenfrequency.
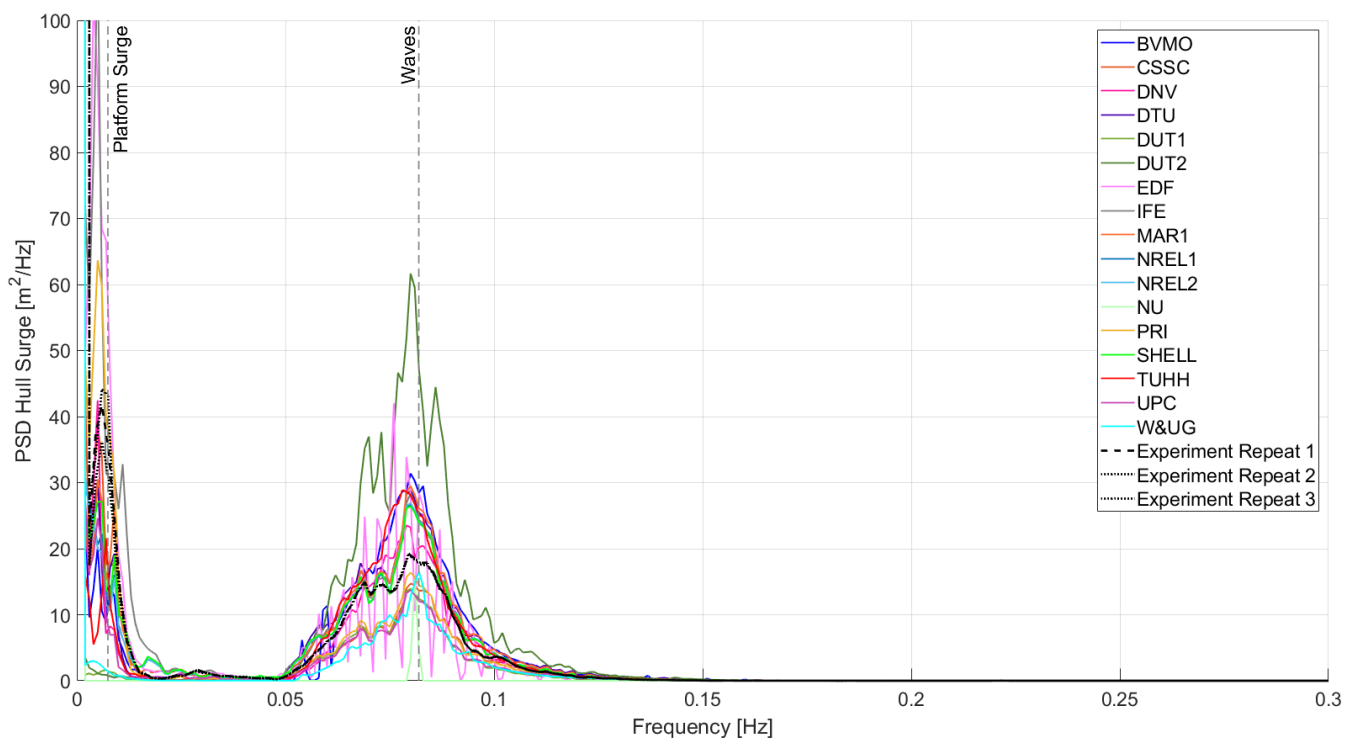
Figure 6: Power spectral density (PSD) of the hull surge motion for the combined wind and wave condition in Load Case 5.3.

430 To compare the system response between participants and against the measurements, the PSD can be integrated (labelled in this paper as a PSD sum) for the linear wave excitation region. This metric is equivalent to the variance (standard deviation squared) over the frequency range of interest and it is related to fatigue loading. Table 6 shows the lower and upper cut-off frequencies for the three irregular waves considered in Load Cases 4.X and 5.X.

Table 6: Lower and upper cut-off frequencies for the linear wave excitation region to compute the PSD sum

435

Load Case	Linear wave excitation region	
	Lower frequency [Hz]	Upper frequency [Hz]
4.2 & 5.2	0.060	0.19
4.3 & 5.3	0.046	0.15
4.4 & 5.4	0.040	0.15

Figure 7 shows the hull surge PSD sum for the different numerical models categorized according to the hydrodynamic theory used (e.g., ME, PF). In this case there are no outputs available from the CFD model (MAR2). Figure 7 also includes the results from three repeats performed during the testing. Similar to Load Case 4.1, the system response in the wave linear region in Load Cases 5.2, 5.3, and 5.4 is governed by the hydrodynamic inertia component. In Load Case 5.2, the hydrodynamic drag
440 slightly increases the wave loading excitation, while in Load Cases 5.3 and 5.4, it provides some damping to the system. All participants using the PF approach, except NU, accounted for the viscous drag contribution by means of Morison-based members. However, the different behavior observed in Figure 7 for NU is not due the lack of viscous drag but rather something not properly set up in the numerical model.
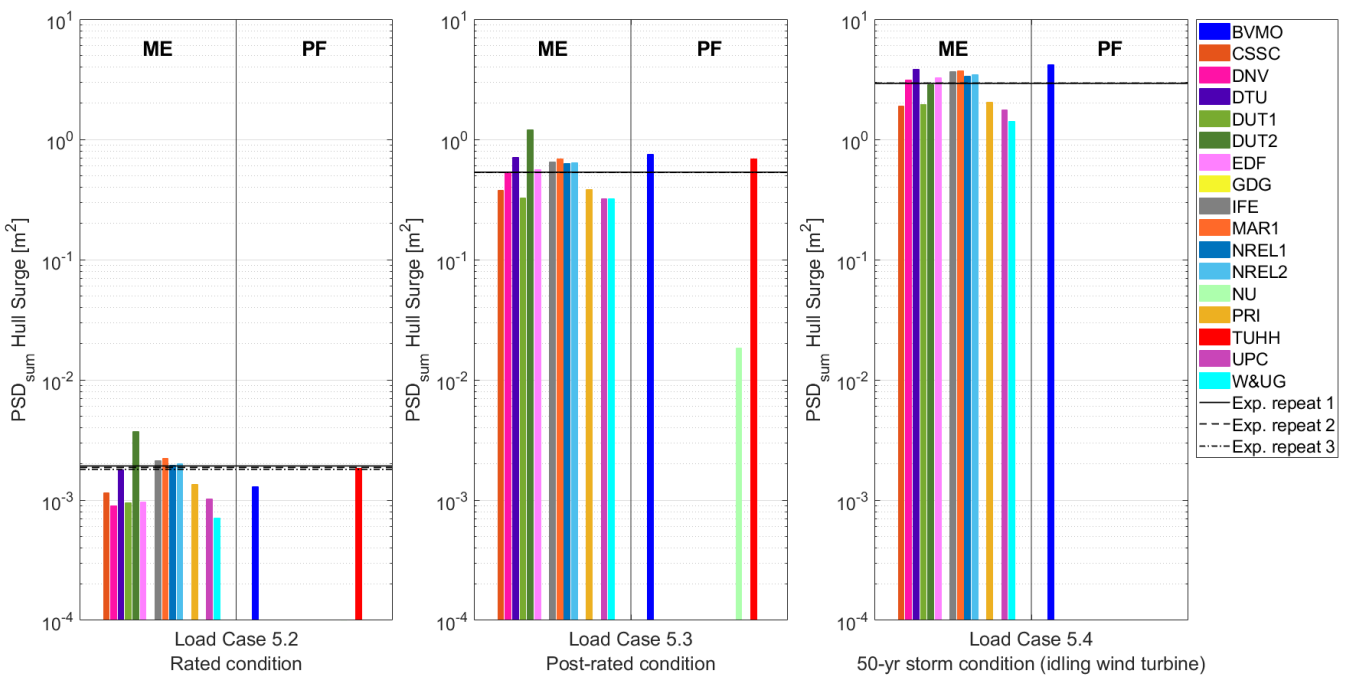
445 **Figure 7:** **Power spectral density (PSD) sum in the hull surge motion for the combined wind and wave conditions in Load Cases 5.2, 5.3, and 5.4. Outputs sorted out according to the hydrodynamic theory: Morison equation (ME) and potential flow (PF). Vertical axis in logarithmic scale.**

Figure 8 and Figure 9 provides the PSD sum for the hull heave and hull pitch motions. Similar to the regular wave condition (Figure 5), most participants tend to underpredict the hull pitch motion when considering the irregular wave conditions (Figure

450 9).

As Figure 7, Figure 8, and Figure 9 shows, Load Case 5.4 (50-yr storm) results in the largest dynamic loading in the linear wave region and Load Case 5.2 (rated condition) in the smallest dynamic loading. As expected, the PSD sum is larger for the higher waves.

Although not shown, the system response in the wave linear region is very similar between the conditions without wind (Load

455 Cases 4.X) and with wind (Load Cases 5.X) with only some relatively small differences in the pitch degree of freedom.
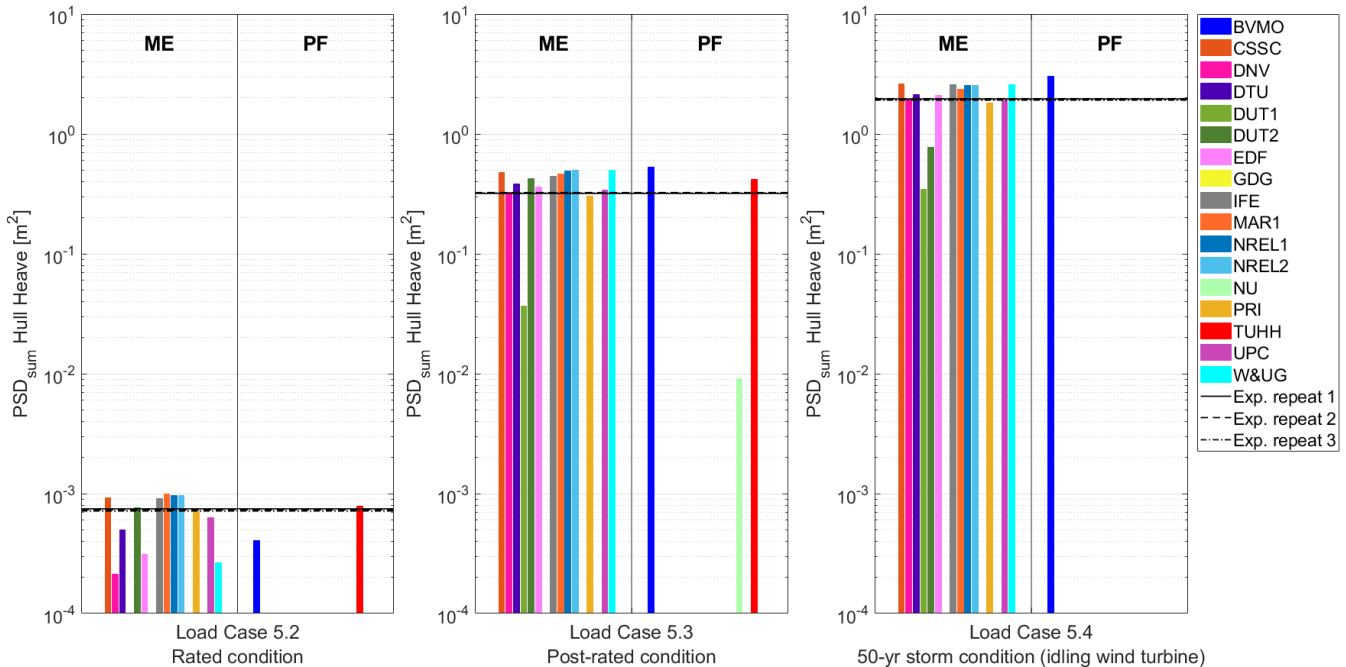
Figure 8: Power spectral density (PSD) sum in the hull heave motion for the combined wind and wave conditions in Load Cases 5.2, 5.3, and 5.4. Outputs sorted out according to the hydrodynamic theory: Morison equation (ME) and potential flow (PF). Vertical axis in logarithmic scale.
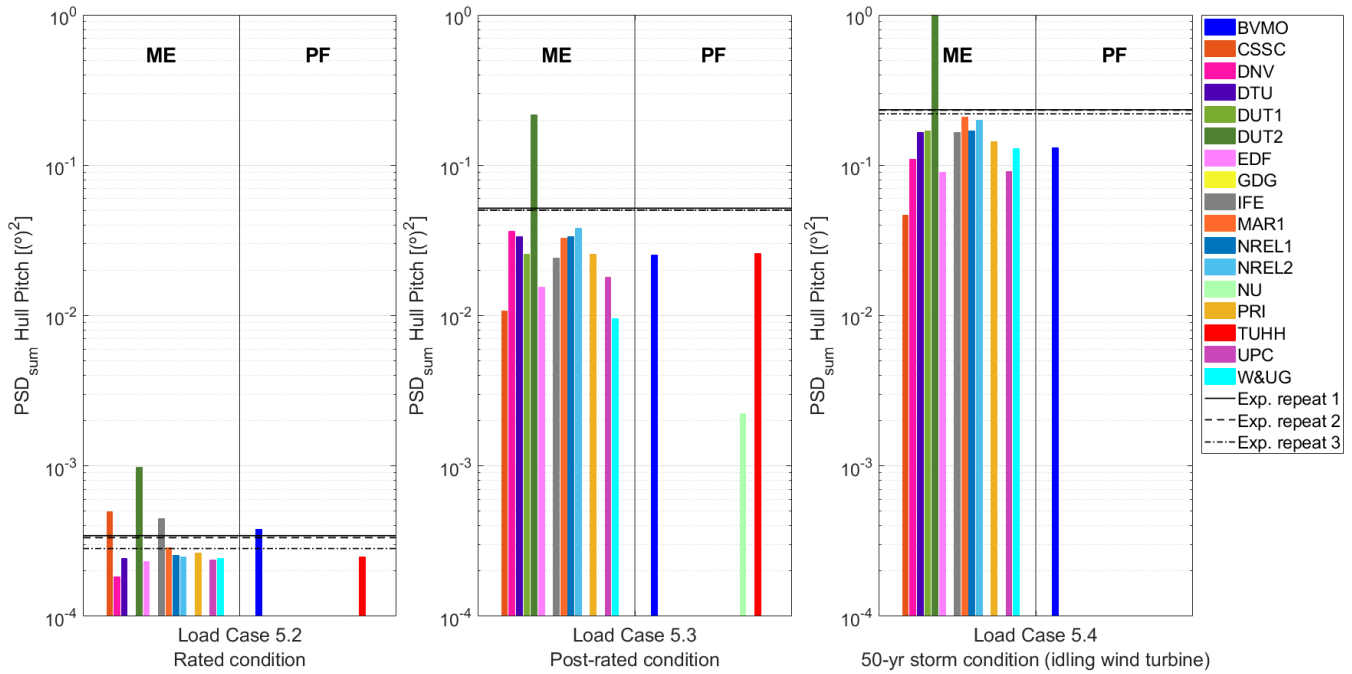
460

Figure 9: Power spectral density (PSD) sum in the hull pitch motion for the combined wind and wave conditions in Load Cases 5.2, 5.3, and 5.4. Outputs sorted out according to the hydrodynamic theory: Morison equation (ME) and potential flow (PF). Vertical axis in logarithmic scale.

5.3 Tower Base Fore-Aft Bending Moment

465   The fore-aft and side-to-side bending moments at the tower base were measured during the testing. The wind and wave load excitations occur at a frequency significantly lower than the first tower bending mode. Figure 6 shows the PSD of the tower-base fore-aft bending moment for an irregular wave-only condition (Load Case 4.3).
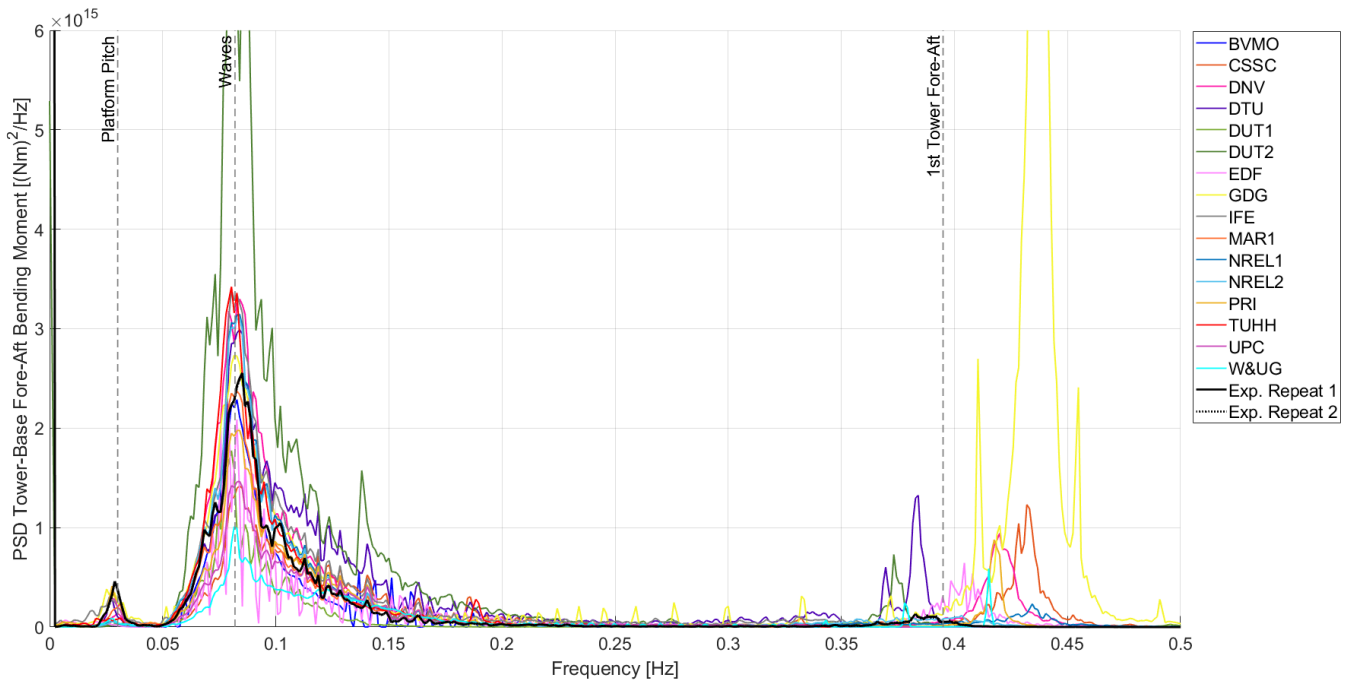
Figure 10: Power spectral density (PSD) of the tower-base fore-aft bending moment for the wave-only condition in Load Case 4.3.

470   For the experiment, the first tower fore-aft bending mode in free-floating conditions occurs at around 0.39-0.40 Hz. Most numerical models properly reproduced the expected frequency for the first tower-bending eigenfrequency for the cantilevered condition (0.34-0.35 Hz). However, when moving to the free-floating conditions, most numerical models tend to slightly overestimate the tower-bending eigenfrequency.

Figure 10 also shows some Morison-only models overestimating the response at the first tower-bending mode. The Morison

475   equation is only valid for diameter to wavelength ratios smaller than 0.2. Otherwise, diffraction effects become significant. To avoid this, the MacCamy and Fuchs diffraction correction of the inertia coefficient (C_m) can be applied (MacCamy and Fuchs, 1954). Alternatively, if this capability is not available in the code used, a low pass filter to the irregular wave spectrum could be used. For the TetraSpar design studied in this project, the largest diameter (4.3 m) corresponds to the central column, hull tri braces, and keel tri braces. Considering deep water conditions and the largest diameter being 4.3 m, the Morison equation

480   without any corrections would overestimate the loading above 0.27 Hz.

Figure 11 shows the PSD sum for the different numerical models categorized according to the hydrodynamic theory used (e.g., ME, PF). In this case there are no outputs from the CFD model because the numerical model from MAR2 accounts for rigid body motion and the loading at the tower base is not available. Figure 11 also includes the results from two repeats performed during the testing.
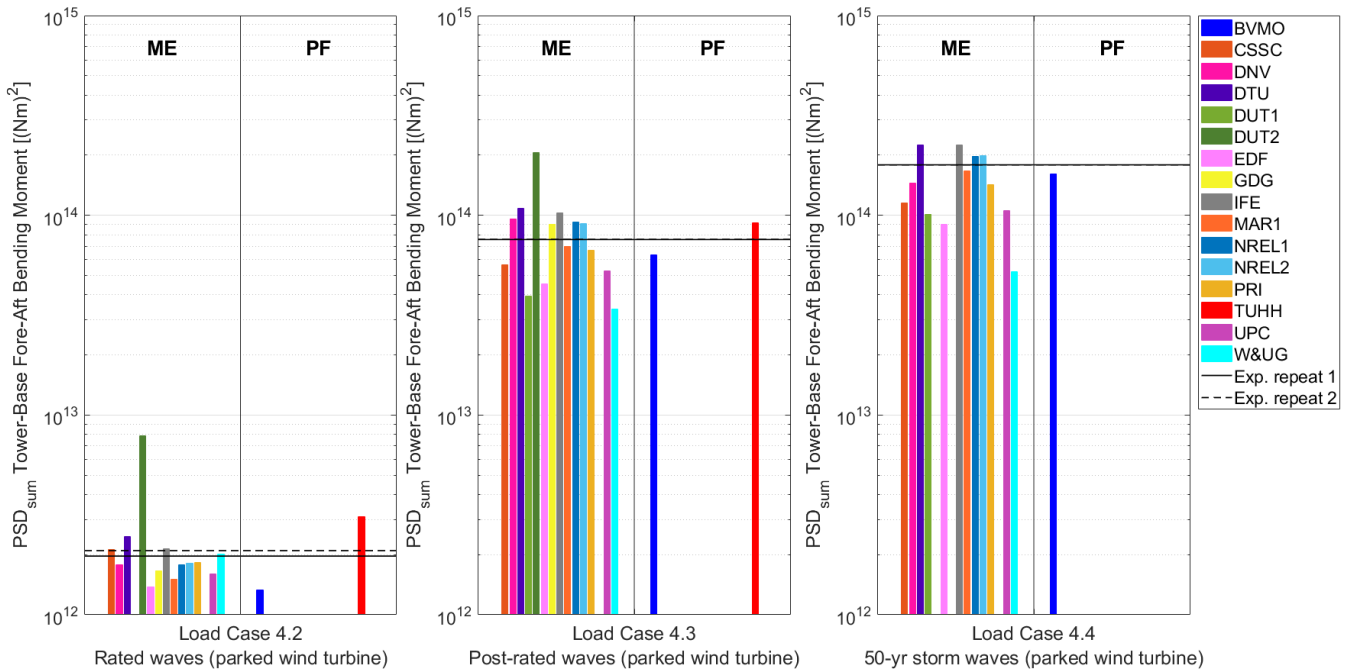
485

Figure 11: Power spectral density (PSD) sum in the fore-aft tower-base bending moment for the wave-only conditions in Load Cases 4.2, 4.3, and 4.4. Outputs sorted out according to the hydrodynamic theory: Morison equation (ME) and potential flow (PF) with augmented viscous drag. Vertical axis in logarithmic scale.

5.3 Upwind Fairlead Tension

490 In slack catenary mooring lines, the fairlead mean tension is determined by the suspended line net weight. When an external force is applied over the wind turbine, the floating system experiences a motion that changes the suspended weight at each line. This results in a new fairlead orientation and tension relative to the unloaded state. By projecting the three fairlead tensions in the horizontal plane, the resultant force that opposes the external forces over the system in that plane could be determined. Figure 12 shows the fairlead tension for the three mooring lines in the system equilibrium condition (Load Case 1.1). As Figure 495 12 shows, the fairlead 2 tension is significantly higher (+80 %) than the tension in the other two fairleads. The reason is that the umbilical cable pulls the system significantly downwind, loading mooring line 2 and unloading mooring lines 1 and 3. This behavior is properly reproduced by the numerical models. Figure 12 also shows a large dispersion for the fairlead 2 measurement as a consequence of the different system resting positions experienced during the testing.
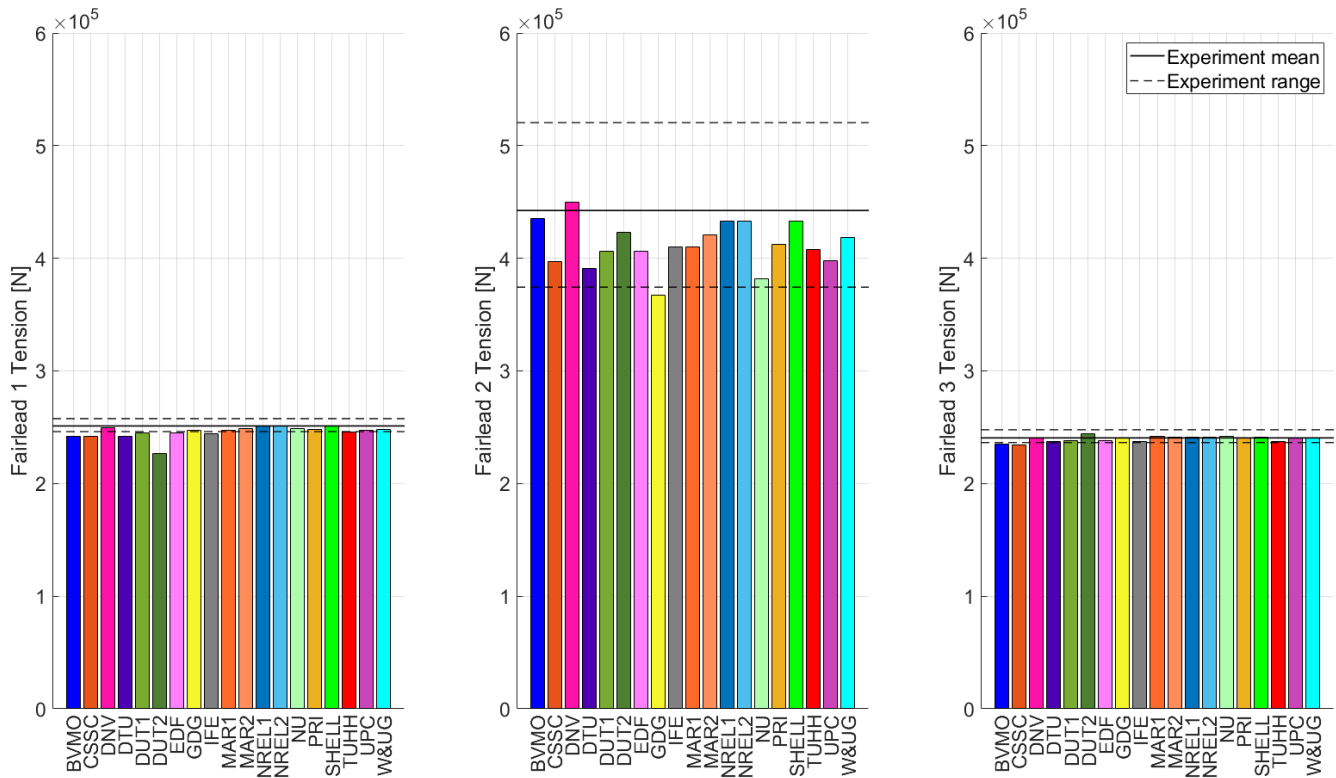
Figure 12: Fairlead tension in the three mooring lines for the system equilibrium condition (Load Case 1.1).

In Load Cases 5.X, the system is loaded by wind and waves. For these conditions, the new fairlead tensions are mainly driven by the aerodynamic thrust force that translates into a platform surge offset. In Load Cases 5.X, the wind is applied along the X-direction. This results in a significant increase in the fairlead 2 tension (located upwind) while the fairlead tension in lines 1 and 3 (located downwind) tend to slightly decrease. Figure 13 shows the mean fairlead tension for mooring line 2 in Load Cases 5.2, 5.3, and 5.4. As expected, Load Case 5.2 (rated condition) results in the highest fairlead 2 mean tension because the aerodynamic rotor thrust is maximum.

For the numerical models, the fairlead 2 mean tension in Load Case 3.1 (steady wind-only condition) shown in Figure 3 is aligned with the fairlead 2 mean tension in Load Case 5.2 (combined unsteady wind and waves) shown in Figure 13. This confirms that the fairlead 2 mean tension is driven by the aerodynamic loading. Interestingly, the experiment shows lower fairlead 2 mean tensions in Load Case 5.2 (see Figure 13) compared to Load Case 3.1 (see Figure 3) and certain dispersion between the repeats during the testing. This again may be related to the uncertainty in the system resting position.

Figure 13 also shows that in Load Case 5.2, the fairlead 2 mean tension recorded during the testing is higher than for most of the numerical models. This indicates that during the testing, the platform experienced a higher mean surge position when the system was loaded.

The experiment shows similar fairlead 2 mean tension in Load Case 5.3 (post-rated condition) and Load Case 5.4 (50-yr storm condition) while the numerical models tend to have slightly smaller fairlead 2 mean tension in Load Case 5.4. For reference, during the storm with the wind turbine in idling conditions, the aerodynamic rotor thrust is similar to the tower aerodynamic drag. It may be that the umbilical induces some additional aerodynamic drag force that becomes significant due the high wind

520   speed. This aerodynamic contribution from the umbilical is not accounted for in the numerical models.

As expected, there are no differences between quasi-static or dynamic mooring lines to estimate the mean line tension.
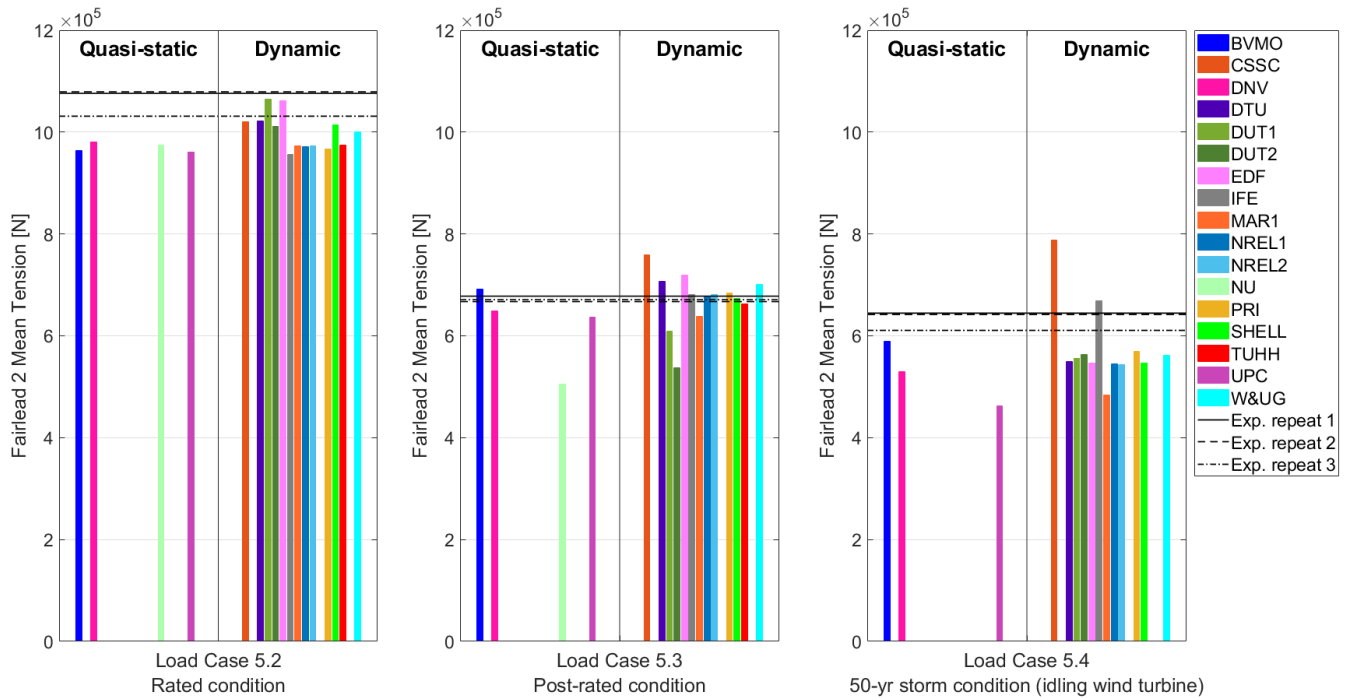
Figure 13: Fairlead 2 mean tension for the combined wind and wave conditions in Load Cases 5.2, 5.3, and 5.4. Outputs sorted out according to the mooring line theory: quasi-static and dynamic.

525   During dynamic conditions, the line load variations are determined by the system motion and the corresponding suspended line weight, inertial loads, hydrostatic loads, hydrodynamic loads of the line moving through the water, and hydrodynamic loads due to the wave kinematics. For example, higher hydrodynamic drag and added mass coefficients along the mooring lines would result in higher loads at the fairlead connections. Quasi-static mooring line approaches only capture changes in the suspended line weight, missing the inertial and hydrodynamic load contributions. Therefore, the quasi-static approach should

530   tend to underpredict the dynamic line loads as observed in OC5 Phase II project (Robertson, 2017).

Figure 14 shows the PSD of the fairlead 2 tension for the combined wind and wave condition in Load Case 5.3. In the very low frequency range, activity can be observed around the platform surge, heave, and pitch frequencies. For the linear wave region, large differences between numerical models are observed.

The response from DUT2 shows two peaks around two and three times, respectively, the peak-spectral wave frequency.
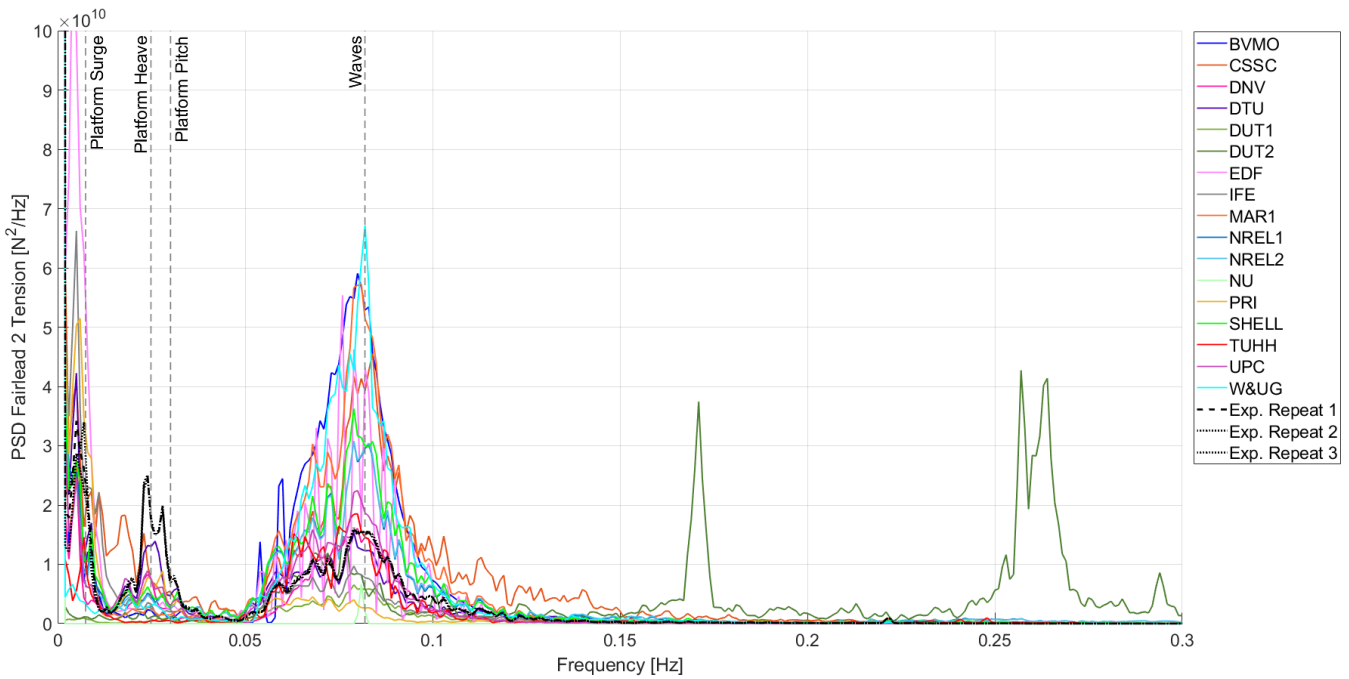
Figure 14: Power spectral density (PSD) of the fairlead 2 tension for the combined wind and wave condition in Load Case 5.3.

Figure 15 shows the PSD sum for the different numerical models categorized according to the mooring line theory used (e.g., quasi-static and dynamic). Figure 15 also includes the results from the three repeats performed during the testing.

As anticipated in Figure 14, there is a significant spread in the outputs from the participants. This indicates that the dynamic loading in the mooring lines driven by the platform motion due to the incoming waves is different between the participants. This might be due to a different platform motion (see Figure 7, Figure 8, and Figure 9) or due to a different line response for a similar platform motion. It is also important to note that different platform mean surge positions (influenced by the umbilical cable) will result in a different suspended line weight, potentially impacting the inertial loading in the mooring lines and resulting in different dynamic forces in the wave region. For example, repeat 3 during the experiment in Load Cases 5.2 and 5.4 returns a lower mean fairlead 2 tension than for the other two repeats (see Figure 13). This is because repeat 3 during the testing experienced a smaller mean platform surge offset. This lower platform offset results in a smaller suspended line length and, therefore, weight, which in turn is likely to induce a lower inertial load. This can be observed in the lower dynamic loading
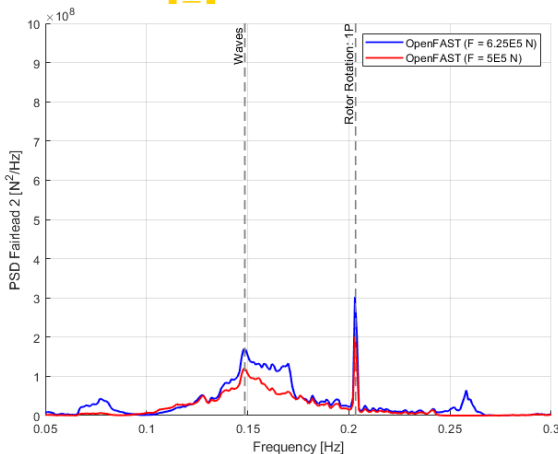
in Load Cases 5.2 and 5.4. Future work could include prescribing the platform to determine if the mooring line responses are similar when the platform the numerical models, the mooring lines length of the upper section were static surge offsets (Wiley et al., 2023). The lengths were extended between were not representative of the physical system.
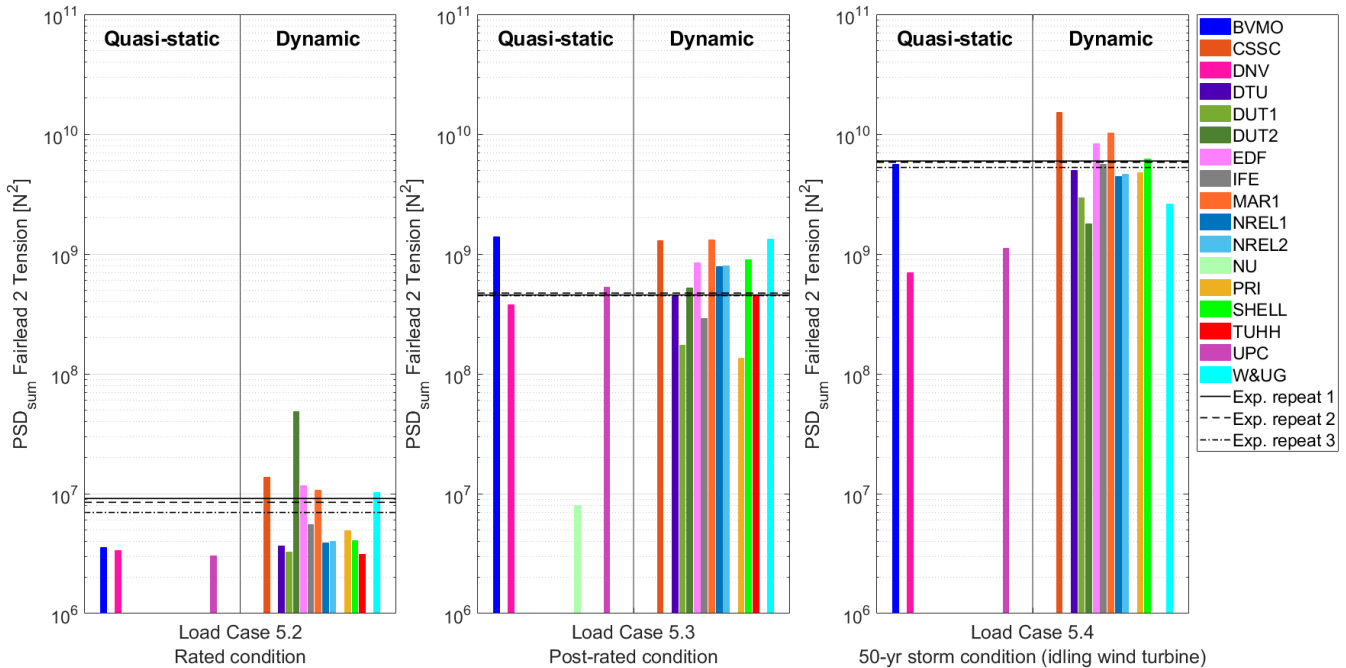
**Figure 15: Power spectral density (PSD) sum in the fairlead 2 tension for the combined wind and wave conditions in Load Cases
5.2, 5.3, and 5.4. Outputs sorted out according to the mooring line theory: quasi-static and dynamic. Vertical axis in logarithmic
scale.**

5.4 Keel Line Tensions

The suspended keel acts as a counterweight providing floating stability to the system. To ensure this floating stability, the six
keel lines must always remain under tension. In these conditions, the two floating support structure bodies (hull and keel)
behave as a rigid body.

The keel line system is statically determinate. The keel lines withstand the net keel weight (i.e., the difference between the
weight of the keel body acting vertically downwards and the hydrostatic buoyancy force acting upwards). The mean tension
at each keel line can be calculated analytically based on the static equilibrium equations (Pereyra, 2018). The keel lines' mean
tension distribution is determined by the roll and pitch rotations of the floating support structure. These rotations are mainly
driven by the RNA overhang and the aerodynamic loading.

Figure 16 shows the tension for each keel line in the equilibrium condition (Load Case 1.1). The disposition of the subplots
follows the physical location of the keel lines shown in Figure 2b. The subplots include the measured mean tension as well as
some small variations that were observed during the testing. Figure 16 also includes for reference the computed tension for
each line based on the analytical approach assuming no platform roll and a platform pitch of -2°. This rotation corresponds to
the equilibrium conditions observed during the testing and is reproduced by most numerical models. There are some differences
between the tensions obtained in the experiment and the ones from the analytical solution. This denotes that some physical
properties in the system may be slightly different.

For the equilibrium condition, the disposition of the floating support structure together with the nacelle oriented along the -X direction results in a symmetric system with respect to the XZ vertical plane (see Figure 2a and Figure 2b for reference). This symmetric nature of the system implies that the loading in the keel lines 1 and 6 are the same, and the same holds true for the pairs of keel lines 2-5 and 3-4, respectively.

There is excellent agreement between most numerical models and the analytical solution. Some participants (EDF, W&UG) show differences in keel line tensions because the system equilibrium position obtained is slightly different (i.e., different platform pitch and/or roll values) while other participants (DTU, DUT1, DUT2) reproduce the expected system rotation but may not have the proper settings in their numerical models (e.g., slightly offset keel line attachment points, line properties or keel net weight).
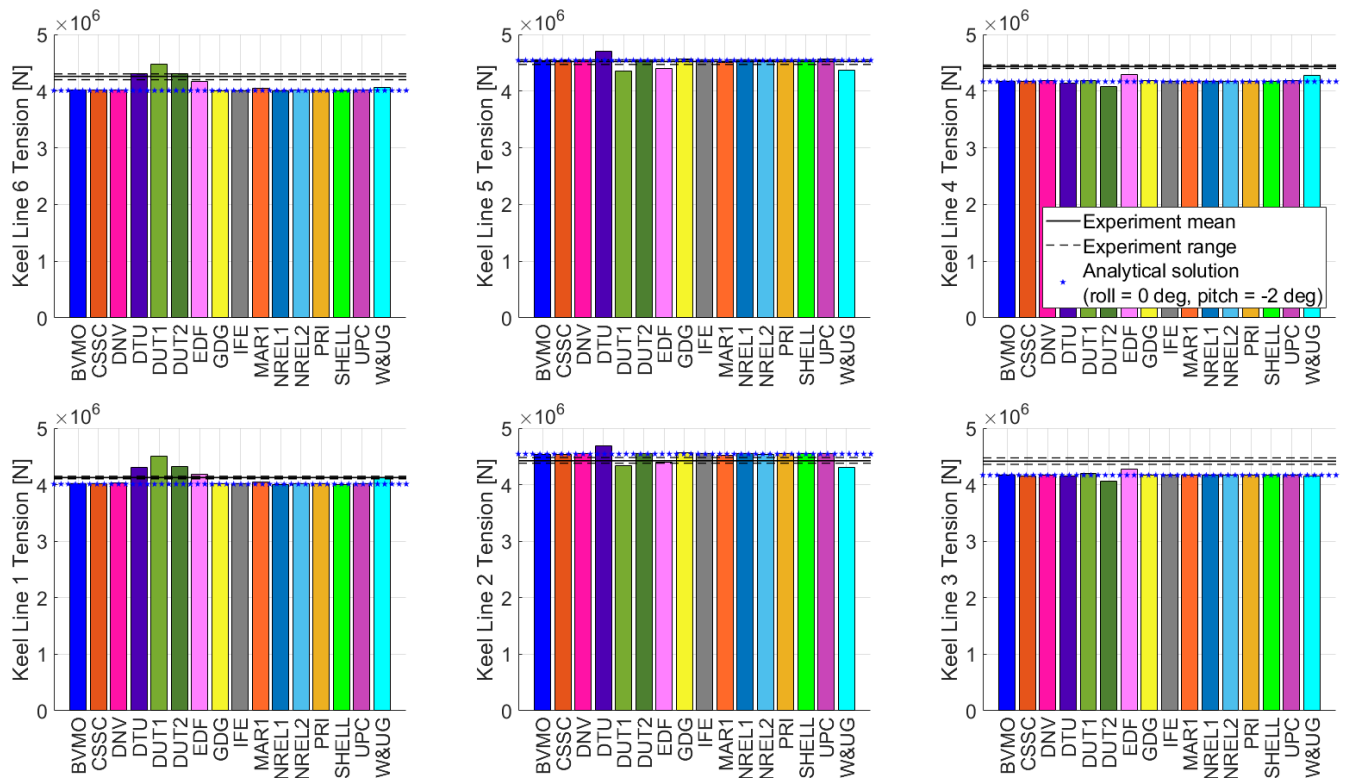
Figure 16: Tension at the six keel lines in equilibrium conditions (Load Case 1.1).

Figure 17 shows the mean tension for each keel line for the combined wind and wave conditions in Load Cases 5.2, 5.3, and 5.4. The symmetric behavior between keel lines is still present in Load Cases 5.2 and 5.3 due to the keel lines disposition around the XZ vertical plane, the nacelle being aligned with the X-axis, and the external loading (i.e., wind and waves) being applied along the X-axis. For these two load cases, the mean keel line tensions are mainly driven by the mean pitch rotation of the floating support structure. Load Case 5.4 (50-yr storm condition) does not exhibit the symmetry around the XZ vertical plane because the system rotates around -2° in roll due to the aerodynamic loading. For this loading condition, the mean keel

590   lines loading is determined by the combination of roll and pitch angles of the floating support structure. For these three load

cases, the analytical formulation was also able to compute the proper mean keel line tensions based on these rotations.
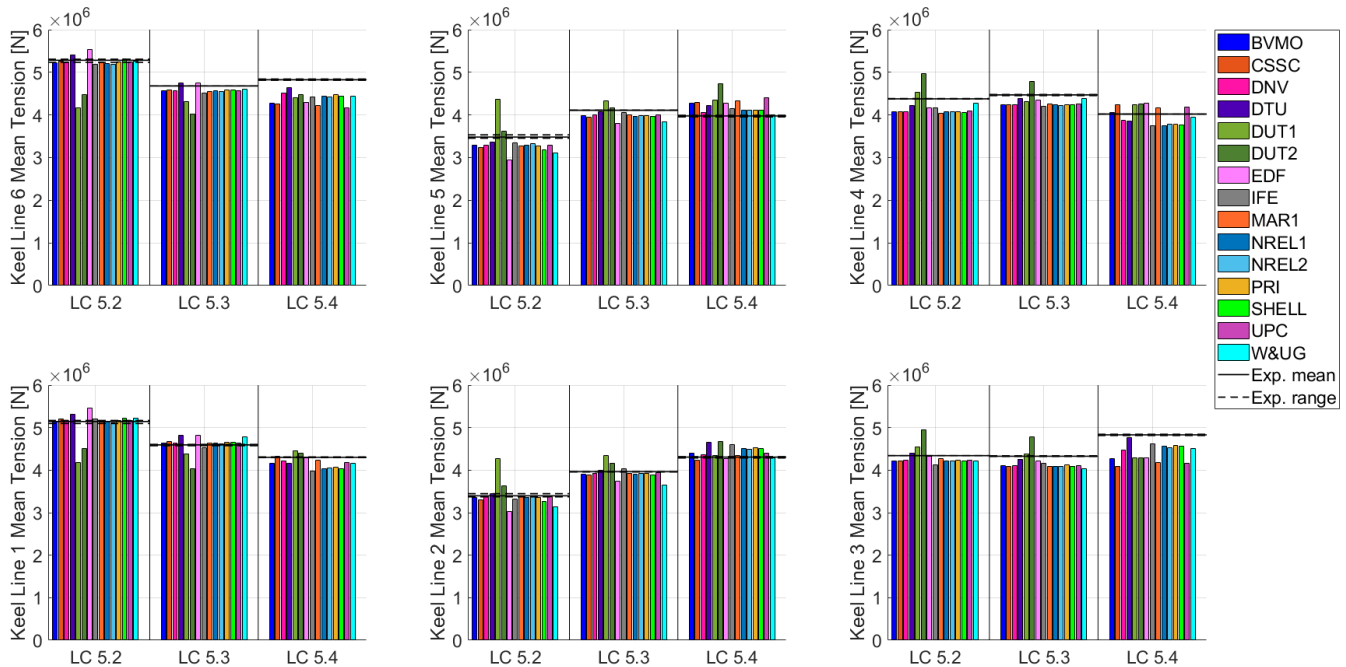
Figure 17: Mean tension at the six keel lines for the combined wind and wave conditions in Load Cases (LC) 5.2, 5.3, and 5.4.

Figure 18 shows the PSD of the six keel lines for the combined wind and waves for the post-rated operating condition (Load

595   Case 5.3). Figure 18 includes the results from the participants as well as the results from three repeats that were performed

during the testing. As expected, the keel lines mainly respond at the linear wave excitation region and, similar to the keel lines

mean tension, exhibit the loading by keel pairs around the XZ vertical plane. The two keel lines located at the downwind side

(i.e., keel lines 3 and 4) experience the smallest dynamic response. The small peak around 0.22 Hz correspond to the 1P

frequency due to a rotor asymmetry (blade mass and blade pitch imbalance).

600   From a modal analysis performed over the numerical models, it was determined that the translational vibration modes of the

suspended keel were located between 1 and 2 Hz and the keel rotational vibration modes between 2.5 and 3 Hz. Despite these

keel natural frequencies being relatively high, the analytical formulation used to estimate the mean keel tensions was not able

to capture the dynamic response. The keel line dynamic response is likely driven by the inertial loading with contributions

from different degrees of freedom (e.g., surge, heave, and pitch) that the quasi-static analytical formulation does not include.

605   This highlights the importance of using higher fidelity models like the ones used by the participants in this project.

Most numerical models are well aligned with the response observed in the experiment. Some participants that had the proper

floating support structure rotations but issues with the keel line tensions in the equilibrium condition (e.g., DUT1 and DUT2),

also exhibit an unexpected dynamic response. This confirms that something is not properly set up in those numerical models.
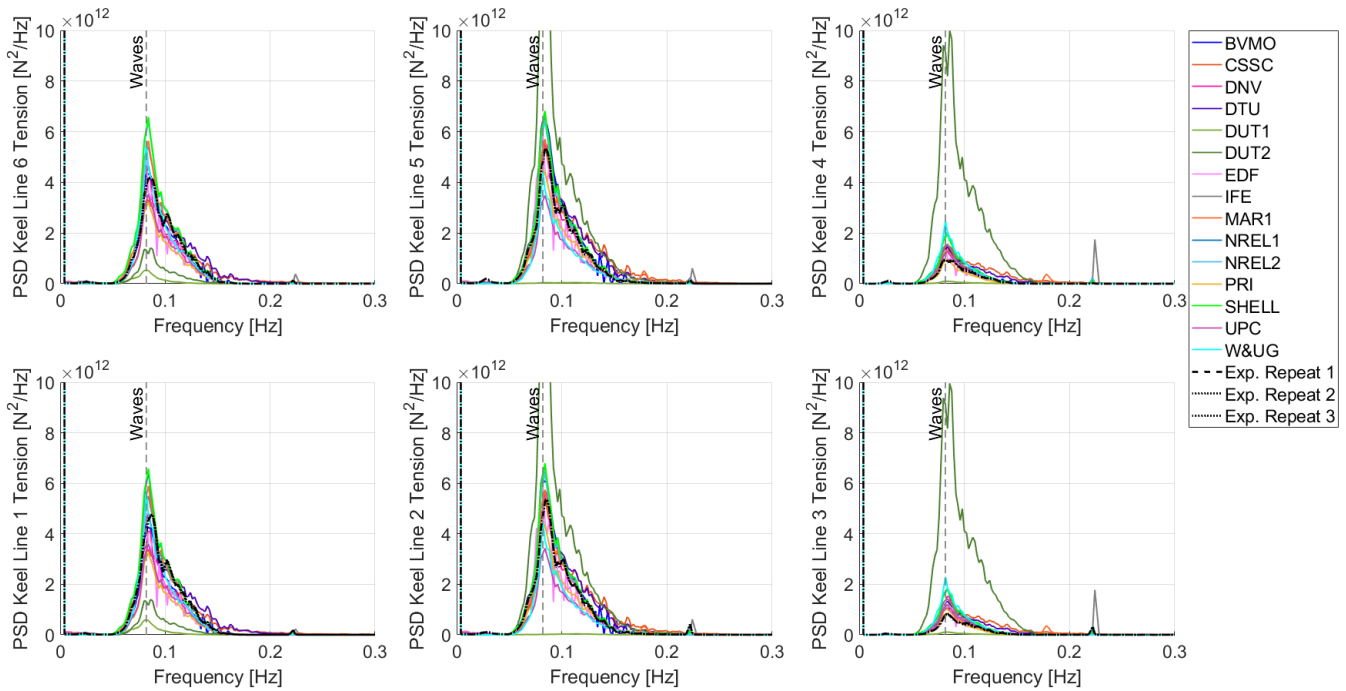
Figure 18: Power spectral density (PSD) for the six keel lines in the combined wind and wave conditions for the post-rated operating condition (Load Case 5.3).

Figure 19 shows the PSD sum for each keel line for the combined wind and wave conditions in Load Cases 5.2, 5.3, and 5.4. As expected, the PSD sum is larger for the higher waves. For example, the PSD sum in Load Case 5.2 (rated condition) is the smallest while the PSD sum in Load Case 5.4 (50-yr storm) is the largest. Similar to Figure 18, it can be observed that the keel lines located at the downwind side always experience the smallest dynamic response.
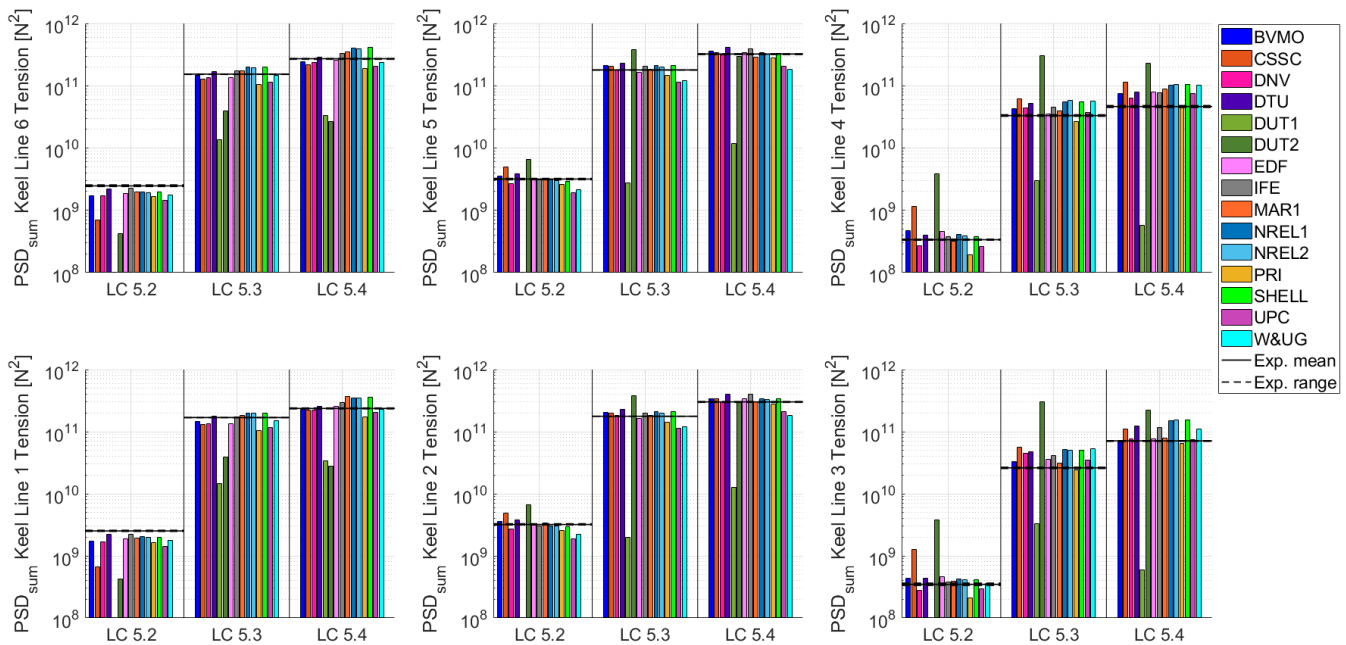
Figure 19: Power spectral density (PSD) sum in the six keel lines for the combined wind and wave conditions in Load Cases (LC) 5.2, 5.3, and 5.4. Vertical axis in logarithmic scale.

6 Conclusions

620   In the frame of the OC6 Phase IV project, participants modeled a 3.6-MW wind turbine atop the TetraSpar floating support structure designed by Stiesdal Offshore Technologies. This configuration is representative of the demonstration project installed in Norway in 2021. Numerical results from participants in the project were compared against measurement data from a 1:43 scale test performed by the University of Maine. The system response was studied under wind, wave, and combined wind and wave conditions. Participants used numerical models of different fidelity levels for the aerodynamics,

625   hydrodynamics, and structural dynamics. During the testing of the floating system, the sensor umbilical used to transfer measurement data and power had an impact in the system equilibrium position and dynamics. Significant changes in the hull surge equilibrium position were observed between tests (between -6.7 m and +6.4 m from the origin of the coordinate system used). Numerical models included the umbilical as an additional line, but there is some uncertainty associated.

Good agreement was observed between the numerical models and the experiment for the aerodynamic loading. The pitch

630   rotation of the floating support structure due to the aerodynamic thrust force did not impact the mean aerodynamic loading. The TetraSpar design is made of slender members. When comparing the Morison equation and potential flow (augmented with viscus drag) approaches, in general, no clear differences were observed. For the wave loading conditions studied, the response of the numerical models based on the Morison equation approach were driven by the hydrodynamic inertia component. The Morison equation approach is only valid for diameters to wavelength ratios smaller than 0.2. To avoid overestimating the

635 response at the first tower-bending mode, numerical models based on the Morison equation approach had to use the MacCamy and Fuchs diffraction correction of the inertia coefficient.

For the combined wind and wave loading, the numerical models showed relatively good agreement for the mean upwind fairlead tension. However, when looking at the dynamic loading, large differences were observed between the numerical models and against the experiment. The response from the numerical models was different even in the linear wave region. The different hull surge equilibrium positions observed during the testing impact the suspended line weight. This results in different mooring line inertial loading when the platform experiences motions and may explain, in part, the different dynamic forces observed in the wave region.

The TetraSpar design is a novel floating support structure that features unique elements like the keel lines. Characterizing the keel line tensions is important because the suspended keel ensures the floating system stability. These tensions can only be

645 obtained by numerical models with the ability to include structural flexibility within the floating support structure. The potential flow (augmented with viscous drag) approach is a viable option to study the keel line loads if the system is discretized into, at least, two potential flow bodies (hull and keel). For the TetraSpar design, the keel lines mean tension can be determined by means of an analytical approach based on static equilibrium equations. The keel lines mean tension changes observed for the different loading conditions are driven by the floating support structure roll and pitch rotations. Good agreement was

650 observed between most numerical models, the experiment, and the analytical approach. The analytical approach (quasi-static) was not able to capture the dynamic response, but the numerical models and the experiment showed very good agreement between them. This accurate estimation of the keel line tensions enables the computation of the fatigue life for these elements. To account for the loading within the hull and keel, it would be necessary to account for the member-level hydrostatics and hydrodynamics. This is the normal procedure for a Morison equation-based approach, but it would challenge the potential flow approach.

Data Availability

The modeling information, the simulation results, and the experimental data from this project will be made available to the public by the end of 2023 through the U.S. Department of Energy Data Archive and Portal, https://a2e.energy.gov/project/oc6.

Author Contributions

660 Amy Robertson: Secured the funding for the OC6 project. Roger Bergua, Will Wiley, Amy Robertson, and Jason Jonkman: Proposed the methodology, formal analysis, and investigation. All authors: Simulated the system and submitted results from their numerical models (detailed in Section 3). Roger Bergua: Postprocessed and visualized the data from the experiment and the numerical models. Roger Bergua: Wrote the manuscript draft. All authors: Reviewed and edited the manuscript.

Competing Interests

665 Some authors are members of the editorial board of Wind Energy Science journal.

Acknowledgements

The authors would like to thank Stiesdal Offshore Technologies, Shell, RWE Renewables, TEPCO RP, and the University of Maine for providing the data to characterize the numerical models and the measurements from the experimental campaign.

670 MARIN would like to acknowledge that their contribution to the project was partly funded by the Dutch Ministry of Economic Affairs.

This work was authored in part by the National Renewable Energy Laboratory, operated by Alliance for Sustainable Energy, LLC, for the U.S. Department of Energy (DOE) under Contract No. DE-AC36-08GO28308. Funding was provided by the U.S. Department of Energy Office of Energy Efficiency and Renewable Energy Wind Energy Technologies Office. The views

675 expressed in the article do not necessarily represent the views of the DOE or the U.S. Government. The U.S. Government retains and the publisher, by accepting the article for publication, acknowledges that the U.S. Government retains a nonexclusive, paid-up, irrevocable, worldwide license to publish or reproduce the published form of this work, or allow others to do so, for U.S. Government purposes.

References

680 Allen, C., and Fowler, M.: 1/4^{3}rd Scale Basin Testing of the 3.6 MW TetraSpar Floating Offshore Wind Turbine–- Spar Configuration. Advanced Structures and Composites Center. University of Maine, 2019.

Babarit, A., and Delhommeau, G.: Theoretical and numerical aspects of the open source BEM solver NEMOH. In Proceedings of the 1^{1t}h European Wave and Tidal Energy Conference (EWTEC2015), Nantes, France. 2015.

Bergua, R., Robertson, A., Jonkman, J., Platt, A., Page, A., et al.: OC6 Phase II: Integration and verification of a new soil–

685 structure interaction model for offshore wind design. Wind Energy, 25(5), pp.793-810. https://doi.org/10.1002/we.2698. 2022a.

Bergua, R., Robertson, A., Jonkman, J., Branlard, E., Fontanella, et al.: OC6 project phase III: validation of the aerodynamic loading on a wind turbine rotor undergoing large motion caused by a floating support structure. Wind Energy Science Discussions, 2022b.

690 Borg, M., Viselli, A., Allen, C.K., Fowler, M., Sigshøj, C., Grech La Rosa, A., Andersen, M.T., and Stiesdal, H.: Physical Model Testing of the TetraSpar Demo Floating Wind Turbine Prototype. In International Conference on Offshore Mechanics and Arctic Engineering. American Society of Mechanical Engineers. https://doi.org/10.1115/IOWTC2019-7561. 2019.

Cioni, S., Papi, F., Pagamonci, L., Bianchini, A., Ramos-García, N., et al.: On the characteristics of the wake of a wind turbine undergoing large motions caused by a floating structure: an insight based on experiments and multi-fidelity simulations from
695 the OC6 Phase III Project, Wind Energ. Sci. Discuss. [preprint], https://doi.org/10.5194/wes-2023-21, in review, 2023.

Craig, R., and Bampton, M.: Coupling of Substructures for Dynamic Analyses. AIAA Journal, Vol. 6, No.7, 1968.

IEA Wind: International Energy Agency Wind Technology Collaboration Programme Task 30, https://www.iea-wind.org/task30/, last access: 3 July 2023.

Jonkman, J., and Musial, W.: Offshore code comparison collaboration (OC3) for IEA Wind Task 23 offshore wind technology
700 and deployment (NREL/TP-5000-48191). National Renewable Energy Laboratory, Golden, CO (United States). 2010. https://doi.org/10.2172/1004009.

Liu, Y.: HAMS: A Frequency-Domain Preprocessor for Wave-Structure Interactions—Theory, Development, and Application. Journal of Marine Science and Engineering. 2019.

MacCamy, R.C., and Fuchs, R.A.: Wave forces on piles: A diffraction theory"" US Army Corps of Engineers, Beach Erosion
705 Board. 1954.

Pegalajar-Jurado, A., Madsen, F.J., and Bredmose, H.: Damping identification of the TetraSpar floater in two configurations with Operational Modal Analysis. In International Conference on Offshore Mechanics and Arctic Engineering. American Society of Mechanical Engineers. 2019.

Pereyra, B.T.: Design of a counter weight suspension system for the Tetraspar floating offshore wind turbine (Master's thesis,
710 NTNU). 2018.

Popko, W., Vorpahl, F., Zuga, A., Kohlmeier, M., Jonkman, J., et al.: Offshore Code Comparison Collaboration Continuation (OC4), Phase I—Results of Coupled Simulations of an Offshore Wind Turbine with Jacket Support Structure (NREL/CP-5000-54124). National Renewable Energy Laboratory, Golden, CO (United States). 2012. https://www.nrel.gov/docs/fy12osti/54124.pdf.

715 Popko, W., Huhn, M.L., Robertson, A., Jonkman, J., Wendt, F., et al.: Verification of a numerical model of the offshore wind turbine from the alpha ventus wind farm within oc5 phase iii. In International Conference on Offshore Mechanics and Arctic Engineering (Vol. 51319, p. V010T09A056). American Society of Mechanical Engineers. 2018. https://doi.org/10.1115/OMAE2018-77589.

Popko, W., Robertson, A., Jonkman, J., Wendt, F., Thomas, P., et al.: Validation of numerical models of the offshore wind
720 turbine from the alpha ventus wind farm against full-scale measurements within OC5 Phase III. In: ASME 2019 38th International Conference on Ocean, Offshore and Arctic Engineering. American Society of Mechanical Engineers Digital Collection. 2019. https://doi.org/10.1115/OMAE2018-77589.

Robertson, A., Jonkman, J., Musial, W., Vorpahl, F., and Popko, W.: Offshore code comparison collaboration, continuation: Phase II results of a floating semisubmersible wind system (NREL/CP-5000-60600). National Renewable Energy Laboratory,
725 Golden, CO (United States). 2013. https://www.nrel.gov/docs/fy14osti/60600.pdf.

Robertson, A.N., Wendt, F.F., Jonkman, J.M., Popko, W., Vorpahl, F., et al.: OC5 project phase I: Validation of hydrodynamic loading on a fixed cylinder (NREL/CP-5000-63567). National Renewable Energy Laboratory, Golden, CO (United States). 2015. https://www.nrel.gov/docs/fy15osti/63567.pdf.

Robertson, A.N., Wendt, F.F., Jonkman, J.M., Popko, W., Borg, et al.: OC5 Project Phase Ib: validation of hydrodynamic
730   loading on a fixed, flexible cylinder for offshore wind applications (NREL/JA-5000-66648). National Renewable Energy Laboratory, Golden, CO (United States). 2016. https://doi.org/10.1016/j.egypro.2016.09.201.

Robertson, A.N., Wendt, F., Jonkman, J.M., Popko, W., Dagher, H., et al.: OC5 project phase II: validation of global loads of the   DeepCwind   floating   semisubmersible   wind   turbine.   Energy   Procedia,   137,   pp.38-57. https://doi.org/10.1016/j.egypro.2017.10.333. 2017.

735   Robertson, A.N., Gueydon, S., Bachynski, E., Wang, L., Jonkman, J., et al.: OC6 Phase I: Investigating the underprediction of low-frequency hydrodynamic loads and responses of a floating wind turbine. In Journal of Physics: Conference Series (Vol. 1618, No. 3, p. 032033). 2020. https://www.nrel.gov/docs/fy20osti/76210.pdf.

Sharma, J.N., and Dean, R.G. Second-order directional seas and associated wave forces. Society of Petroleum Engineers Journal, 21(01), pp.129-140. 1981. https://doi.org/10.2118/8584-PA.

740   Stiesdal Offshore Technologies. The TetraSpar Full-Scale Demonstration Project,   https://www.stiesdal.com/offshore-technologies/the-tetraspar-full-scale-demonstration-project/, last access 5 April 2022.

University of Maine. Alfond W^2 Ocean Engineering Lab, https://composites.umaine.edu/facilities/w2/, last access 10 April 2022.

Thomsen, J.B., Têtu, A., and Stiesdal, H.: A comparative investigation of prevalent hydrodynamic modelling approaches for
745   floating offshore wind turbine foundations: a TetraSpar case study. Journal of Marine Science and Engineering, https://doi.org/10.3390/jmse9070683. 2021.

Lee, C.H., and Newman, J.N.: WAMIT User Manual; WAMIT, Inc.: Chestnut Hill, MA, USA, 2006.

Wang, L., Robertson, A., Jonkman, J., Yu, Y.H., Koop, A., et al.: OC6 Phase Ib: Validation of the CFD predictions of difference-frequency wave excitation on a FOWT semisubmersible. Ocean Engineering, 241, p.110026. 2021.
750   https://doi.org/10.1016/j.oceaneng.2021.110026.

Wiley, W., Bergua, R., Robertson, A., Jonkman, J., and Wang, L.: Definition of the SOT TetraSpar Floating Wind System for OC6 Phase IV (NREL/TP-5000-XXXXX). National Renewable Energy Laboratory, Golden, CO (United States). In review, 2023.